Chapter 4

Application of Proton Beam Fabricated Biochips for Single Cell Electroporation

Among all the cell transfection techniques, cell electroporation is considered the transfection technique with high success rate. Studying the individual cells can provide a wealth of information and insight typically obscured by bulk measurements. However, in order to achieve the information of the single cells, the proper design, fabrication technique and instruments have to be studied. Here, we report the single cell electroporation using proton beam fabricated biochips. In this chapter, the design and fabrication for the biochips are described. The electrode fabrication protocols on glass substrate are also mentioned. Followed which the new electroporation system setup and methods for our biochip experiments are introduced. The optimization results, conclusions and comments are reported in the last part of this chapter.

4.1 Biochips design for Single cell Electroporation purpose

Electroporation is the transfection technique using quick electrical pulses to stimulate cells to open their membrane pores. The pulses are normally given through parallel conductive electrodes which the cells are placed in between. Since the electrical pulses play the most important role in this technique, the design of the device and electrode then become crucial, and a well designed device will lead to the successful results. Here we present the design of our novel electroporation biochip for single cell electroporation (figure 4.1). The device is made on a circular glass substrate which is compatible with cell adhesion and growth, and incorporates micron-size conductive electrodes. The biochip is designed to be easy to use, and also reusable.

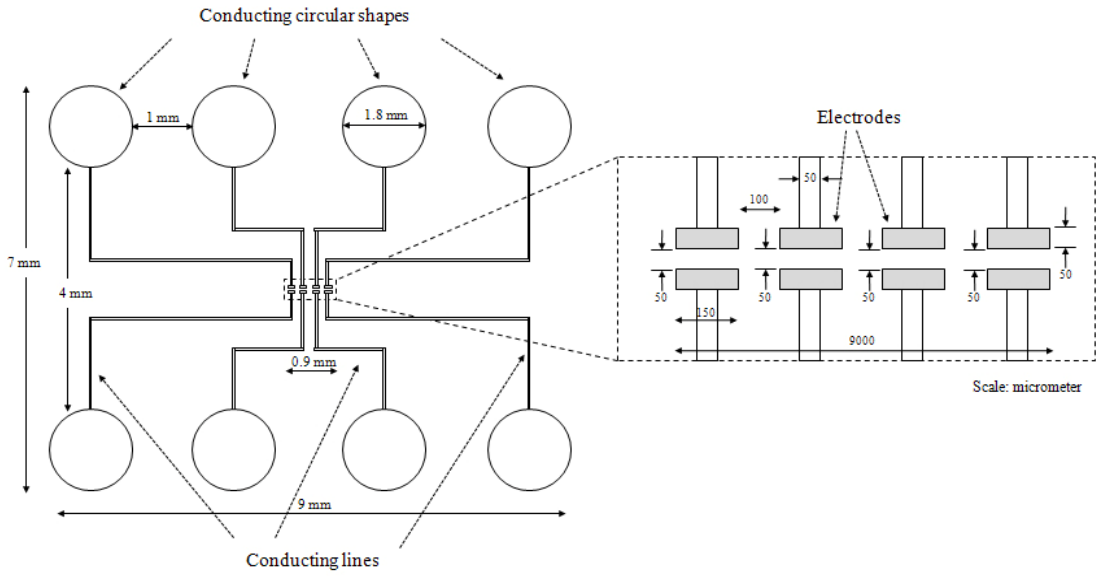

Figure 4.1 Design of the biochips for single-cell electroporation. The structure consists of 8 conducting circular shape pads linked to 4 electrode pairs in the centre of the chip with conducting lines. The electroporation experiments are conducted on adherent cells between the electrodes.

The biochip consists of eight conducting 1800-μm-diameter circular pads used for external contact with electric probes (shown in figure 4.1). The circular pads are connected to the electrodes via 50-μm wide conducting lines. The gap between each pair of electrodes is 50 μm and is fabricated by PBW in order to achieve high aspect ratio and straight-sided wall structures. The 50 μm-electrode gap is compatible with single cell electroporation of Mouse Neuroblastoma (N2a) cells which are normally about 10 μm in size; therefore, the cells will be able to grow comfortably without squeezing or overlapping with each other when they are in between the electrodes. Another advantage of the small gap size is that low applied electrode voltages are sufficient to electroporate cells.

Two lithographic techniques, standard UV lithography and PBW, were involved in the chip fabrication. The more precise PBW method was used to fabricate the 4 pairs of the electrodes at the centre of the biochip. The other parts, circular pads and conducting lines, were not fabricated by PBW since precise geometry and sidewall quality was not necessary for these parts. UV lithography was therefore used in the fabrication of these areas. Further details about the fabrication will be described in the next section.

4.2 Biochip fabrication

In this section, all the preparation techniques and procedures for biochip fabrication will be described in detail starting from substrate preparation, sputtering technique, and nickel electroplating technique as well as further details involving PBW, e.g. image file preparation, which was not mentioned in the previous chapter. The entire process for biochip fabrication is summarized in figure 4.6.

4.2.1 Nickel electroplating

The conductive parts and the electrodes on the biochip are designed to be ~ 7 μm thick. In order to provide electric pulses between the electrode plates, the electrodes have to be conductive, and the conducting parts are fabricated from the PBW exposed resist templates. Electroplating is the technique used to deposit specific material such as Nickel (Ni) or Copper (Cu) to form the conducting structures. Among all the deposited materials, Ni has been commonly used for electroplating due to its excellent electroplating properties. The aqueous-metal solution is typically made of nickel, Ni^{2+}, hydrogen, H^+ and sulphate ions, SO_4^{2-}. Ni ions are attracted to the negatively biased cathode and receive free electrons upon their arrival. The Ni ions are converted into metallic nickel and deposit at the cathode surface to form a thin Ni layer. Meanwhile, the nickel anode (sulphur depolarised nickel pellets loaded into titanium basket) is consumed to replenish the plating solution of the ions through electrochemical etching. The plating process may also produce hydrogen gas because hydrogen ions also gain electrons from the cathode and form bubbles. This is an undesired product as the bubbles can obstruct

the deposition thereby lowering the plating efficiency. Figure 4.2 illustrate typical setup for nickel electroplating.

The electroplating requires the sample to have an adequate metallic seed layer. It has been studied by van Kan et al. [30, 34] that protons are not affected by the underlying substrates and no proximity effects have been observed. Therefore, any metallic layers can be used. Our glass cover slip was pre-coated with thin Au and Cr layer to form a conductive layer which is crucial for nickel electroplating.

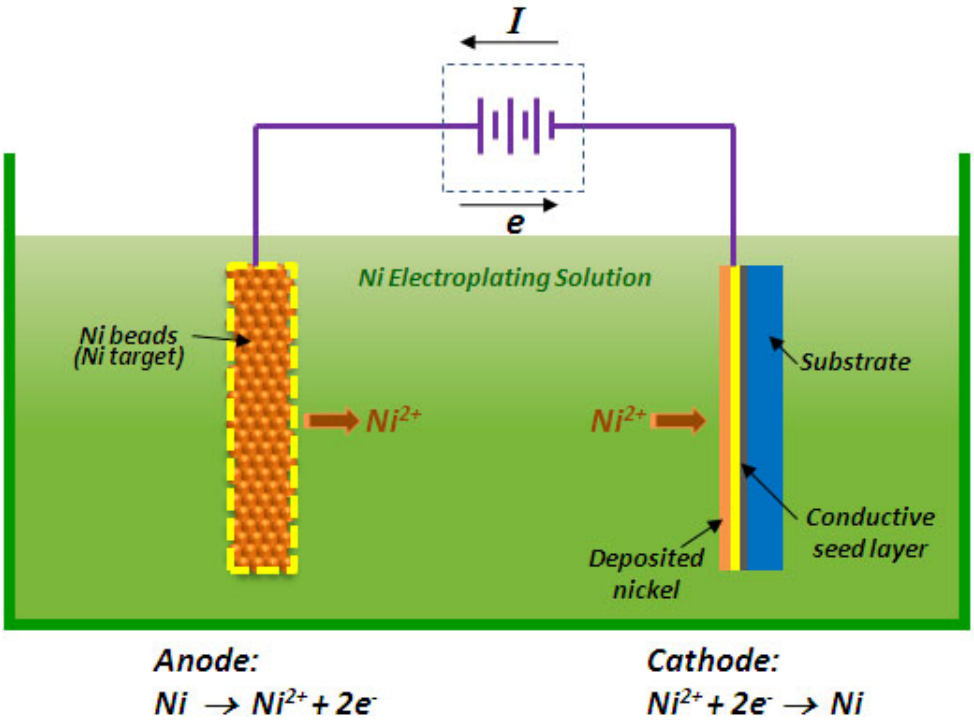

Figure 4.2 Illustration of typical setup for nickel plating. The electrical voltage is given across two electrodes, the nickel pellets are at anode giving Ni^{2+} to the solution while the conductive substrate is at cathode receiving the ion deposited on the surface.

The plating has been carried out using a typical Ni sulfamate bath solution with sodium-dodecyl-ether-sulphate wetting agent and without organic additives using a Technotrans AG, RD.50 plating system installed in the CIBA clean room (1000 P/ft^2). Nickel sulfamate is the primary source of nickel ions (Ni^{2+}); the sulfamate solution is popular in most of the micro-fabrication works. Our electroplating cell contains 100 liters of the plating solution in a poly-propylene electrolyte tank. The processing cell has an anode basket, comprising spherical nickel pellets (INCO S-nickel pellets), which dissolve at nearly 100% efficiency into the electrolyte. A filtration bag is attached to the anode to protect the plating solution from insoluble particles and impure chemicals. A low concentration of nickel chloride is needed to increase anode dissolution and solution conductivity, thereby reducing voltage requirements and improving uniformity of deposition distributions. However, since the chloride is highly corrosive, then in order to protect the anode, a low chloride content should be maintained.

Boric acid in the bath serves as a pH buffering reagent mainly at current densities less than 1.0 A dm^{-2}, and also effectively suppresses hydrogen evolution and helps to suppress the development of high internal stresses in the plated nickel films [117]. Since the cathode efficiency (95-97%) is typically lower than the anode efficiency (approaching 100%), the nickel ion concentration and the pH value will gradually increase during the plating process. Surfactant (sodium laury sulfate) is added as a wetting agent to lower the surface tension of the electrolyte, and to avoid air and hydrogen bubbles attaching to the sample surface.

The temperature and pH can influence the hardness and internal stress of the plated metal. A temperature around 50 – 52^{o}C and pH below 4.0 are necessary for the plating

solutions. In normal conditions, the pH tends to rise hence a regular addition of dilute sulfuric acid (H_2SO_4) is necessary to adjust the pH value. In addition, agitation is also important to dispel bubbles from the cathode surface, which otherwise may cause pitting in the formed Ni structures.

Faraday's law

Faraday's law states that the amount of electrochemical reaction that occurs at an electrode is proportional to the quantity of electric charge Q passed through an electrochemical cell. Thus if the weight of a product of electrolysis is m then Faraday's law states that

$$m = ZQ \tag{4.1}$$

Where Z is the electrochemical equivalent, the constant of proportionality. Since Q is the product of the current I in amperes, and the elapsed time t, in seconds,

$$Q = It \tag{4.2}$$

$$m = ZIt \tag{4.3}$$

According to the Faraday's law the production of one gram equivalent of a product at the electrode, W_{eq}, in a cell requires 96,487 coulombs. The constant 96,487 is termed the Faraday constant F. The coulomb is the quantity of electricity transported by the flow of one ampere for one second.

The Faraday constant represents one mole of electrons and its value can be calculated from

$$F = N_A e \tag{4.4}$$

Where N_A is Avogadro's number (6.0225×10^{23} molecules/mol) and e is the charge of a single electron (1.6021×10^{-19} coulombs, C)

One equivalent, m_{eq}, is the fraction of a molar (atomic) unit of reaction that corresponds to the transfer of one electron. In general,

$$m_{eq} = \frac{A_w}{n_{el}} \tag{4.5}$$

A_w is the atomic weight of metal deposited on the cathode, and n_{el} is the number of electrons involved in the reaction.

When Q = 1 coulomb, or Q = 1 ampere second, then $m_{Q=1} = Z$. Equation (4.1) becomes

$$m = m_{Q=1} Q \tag{4.6}$$

The value of Z, or $m_{Q=1}$, can be evaluated in the following way. Since 96,487 coulombs are required for the deposition of an equivalent of a metal, m_{eq}, from Eq. (4.1) it follows that

$$m_{eq} = 96{,}487\ Z \tag{4.7}$$

And

$$Z = m_{Q=1} = \frac{m_{eq}}{96{,}487} = \frac{m_{eq}}{F} \tag{4.8}$$

Since $m_{eq} = \frac{A_w}{n_{el}}$, Eq. (4.5),

$$Z = \frac{A_w}{n_{el}F} \tag{4.9}$$

Finally, from Eqs. (4.1) and (4.9)

$$m = \frac{A_w}{F \cdot n_{el}} I \cdot t \tag{4.10}$$

In the case of Nickel deposition, m is the amount of mass of Ni deposited at the cathode or dissolved at the anode, A_w is the atomic weight of Ni, n_{el} is the number of electrons involved in the reaction, F= 96487 (C/mol) is Faraday's constant, I is the current flowing through the plating tank, and t is the electroplating time.

The thickness of Ni deposition h is calculated by considering the volume and density ρ, stated as follows,

$$h = \frac{m}{\rho \cdot A} \tag{4.11}$$

where A is the area being electroplated. In practice, side electrochemical reactions may occur such as the formation of hydrogen, which consumes a small portion of the current. Hence, an item of plating efficiency η is introduced to describe the effective performance of current to deposit the metal. The deposited thickness can then be determined by:

$$h = \eta \frac{A_w \cdot I \cdot t}{\rho \cdot A \cdot F \cdot n_{el}} \tag{4.12}$$

and the electroplating rate therefore is derived as,

$$\frac{dh}{dt} = \eta \frac{A_w \cdot J}{\rho \cdot F \cdot n_{el}} \tag{4.13}$$

where J is the current density. With respect to nickel, the atomic weight is 58.69 g/mol, the number of electrons involved n_{el}= 2, and its mass density ρ = 8.9 g/cm^3. The thickness of nickel deposition can be calculated as,

$$h = \eta \frac{58.69}{8.9 \times 96487 \times 2} Jt = \frac{\eta}{29263} Jt \tag{4.14}$$

where h is in cm, J is A/cm^2, and t is in seconds. If we consider current efficiency at the cathode to be 95.5%, with a typical current density of 50 mA/cm^2, then the time required to plate a 7 μm thick nickel film is around 7 minutes.

4.2.2 Substrate preparation

The entire device is fabricated on circular glass cover slip (Fisherbrand® Micrscope cover glass 22 mm diameter). The glass cover slips are suitable for the cell study because it is more compatible for cell adhesion than other substrates. Furthermore, the glass is an insulator which will not interfere with the electric pulses given to the conductive electrodes. The glass also makes the chip easily observed under the inverted microscope because of the transparent property.

Before the fabrication process, the glass cover slip is pre-cleaned with Acetone, Ethanol, and DI water for 10 minutes successively in the sonicator. The cleaning process is taken place in the clean room to prevent any deposited impurities on the surface before the sputtering steps.

4.2.3 Structure patterning

Since the glass substrate is the insulator, a conductive metal layer needs to be coated onto the wafer to serve as a plating seed layer, where nickel could deposit and grow. Here this conductive layer (Au) was deposited on an intermediate layer of chromium (Cr) acting as a layer to improve the adhesion between the gold seed layer and the glass.

To form the gold and chromium films, a Cr and Au target was bombarded with high-energy inert ions in a vacuum chamber operating at a pressure under 5×10^{-3} Torr. Argon ions were produced by glow discharge plasma using DC bias between the sample wafer and the metal target (cathode). The ion bombardment removed individual atoms or clusters from the metal target surface and ejected them towards the wafer, thereby forming a thin metal layer. Empirical evaluation of the plating results suggests that a 20-30 nm Cr layer and 60-200 nm Au layer could provide good adhesion and adequate electric conductivity. In our project, the glass cover slip was sputtered with 20 nm Cr layer and 60 nm Au layer. Although the thick layers may give better adhesion, they will reduce visibility when viewed through a microscope. Therefore, we chose the minimum thickness which gives enough adhesion and conductivity for subsequent electroplating.

Before PMMA was coated, the cover slip was dry baked at 180^{o}C for 20 minutes followed by air cooling for 3 minutes. The PMMA A11 is then spin coated on the substrate twice to form a 7 μm layer, as one coat lays down about 3.5 μm. After that the coated substrate was baked at 180^{o}C for 30 minutes and left to cool to room temperature.

4.2.3.1 UV lithography patterning

The circular contact pads and the conducting lines were patterned on the resist layer by standard UV lithography. The UV lamp (365 nm wavelength) was used as the light source for this step, and all the procedures were done in the CIBA clean room. UV radiation is passed through a quartz photomask, which has the chip pattern formed on its surface, onto a prepared PMMA substrate. The resist is exposed according to the pattern of the transmitted UV radiation.

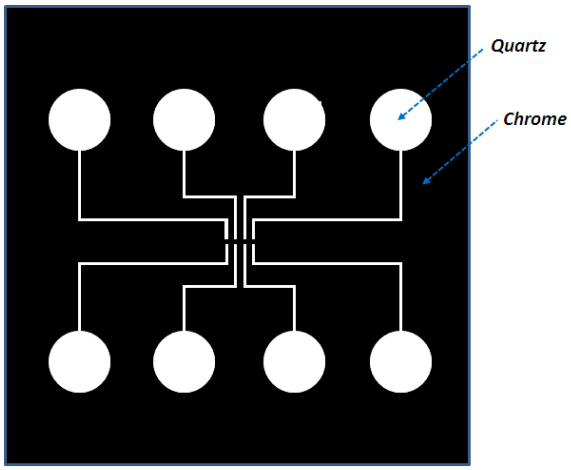

Figure 4.3 UV mask contains structures of circular pads and conducting lines. The structures that are not covered with chrome allow the UV through. Note that the mask pattern does not include the central electrodes since they will be written subsequently by PBW.

The mask pattern used in the UV exposure is shown in figure 4.3. The pattern is derived from the chip design (figure 4.1) but excludes the electrodes, which will be subsequently patterned by PBW. The pattern on the mask was positioned and placed at the centre of the PMMA coated glass cover slip. The PMMA was exposed for 25 minutes

through the patterned mask, which is sufficient for 7 μm thick PMMA. The sample was then developed in an IPA developer for about 5 minutes to remove the exposed PMMA.

4.2.3.2 PBW patterning

The sample that was successfully patterned by standard UV lithography was then subsequently patterned by PBW to form the electrode structures. The size of one electrode is 50 μm (width) × 150 μm (length). Before the scanning, the 1024×1024 pixel image file was created using *Paint* program and transferred to EPL file which can be read by the *Ionscan* program. Figure 4.4 shows the image file which contains a black and white image. The *Ionscan* will control the beam to write over any pixel corresponding to the colour black. The electrode structures were created with a size of 1024 × 341 pixels. Since the scan size was set at 150 μm, the program will then control the beam to write the electrode structure with dimensions of 150×50 micron.

Before the scan, the beam spot position has to be monitored so we can align the electrode structures to the existing connnecting lines previously patterned by UV lithography. Since there were 4 pairs of the electrodes at the centre of the chip, the same EPL file was written 8 times at the different positions (figure 4.4) so that each pair of electrodes is separated by a 50-μm gap.

After the exposure using PBW, the sample was then developed in IPA developer before the electroplating step. Nickel was then electroplated on to the developed pattern at a thickness of around 7 μm. The deposition was carried out employing a current density ~15 mA/cm^2 (for 50 cm^2 exposed area). The current density was varied

depending on the area to be covered, such that a growth rate of 0.5 μm/minute was maintained.

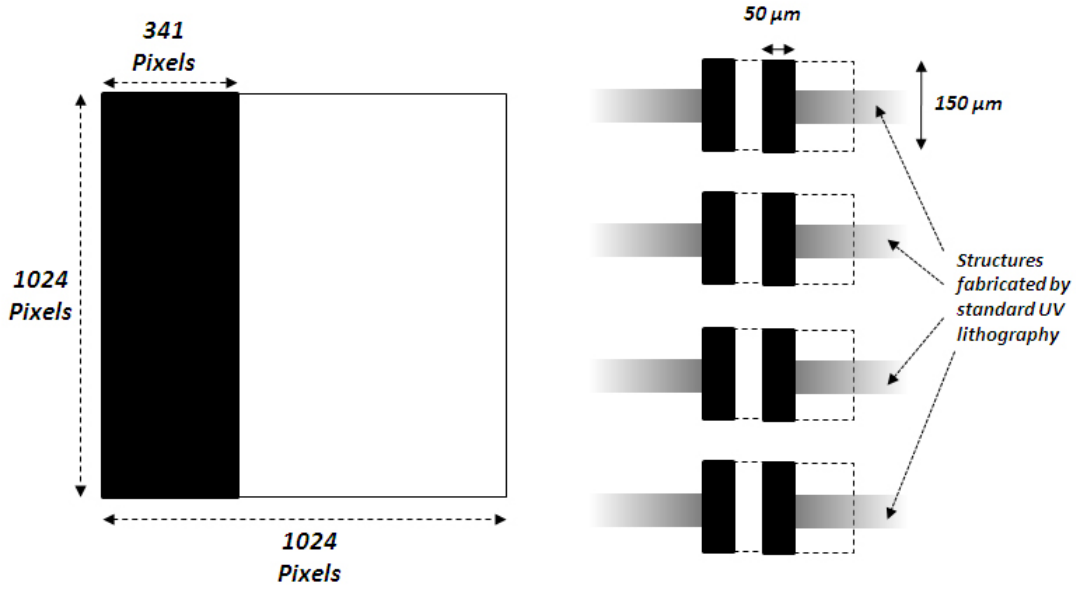

Figure 4.4 The image file created for Ionscan program to write electrode structures on the substrate. The same file was written on one substrate for 8 times, creating 8 electrodes connected to the conducting lines which were patterned by UV lithography.

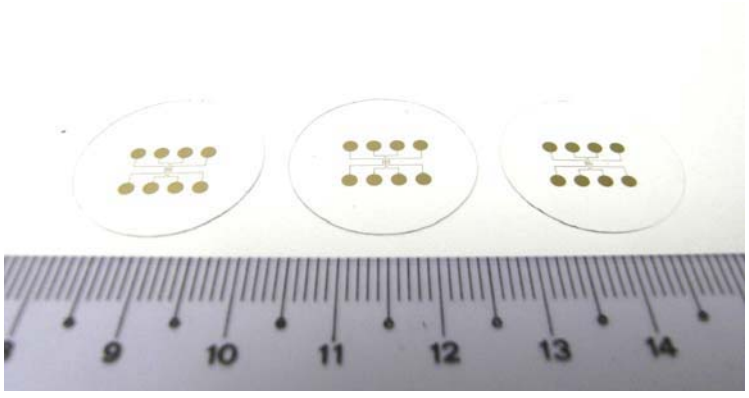

Figure 4.5 The final electroporation biochips ready for cell culture before electropermeabilization experiments.

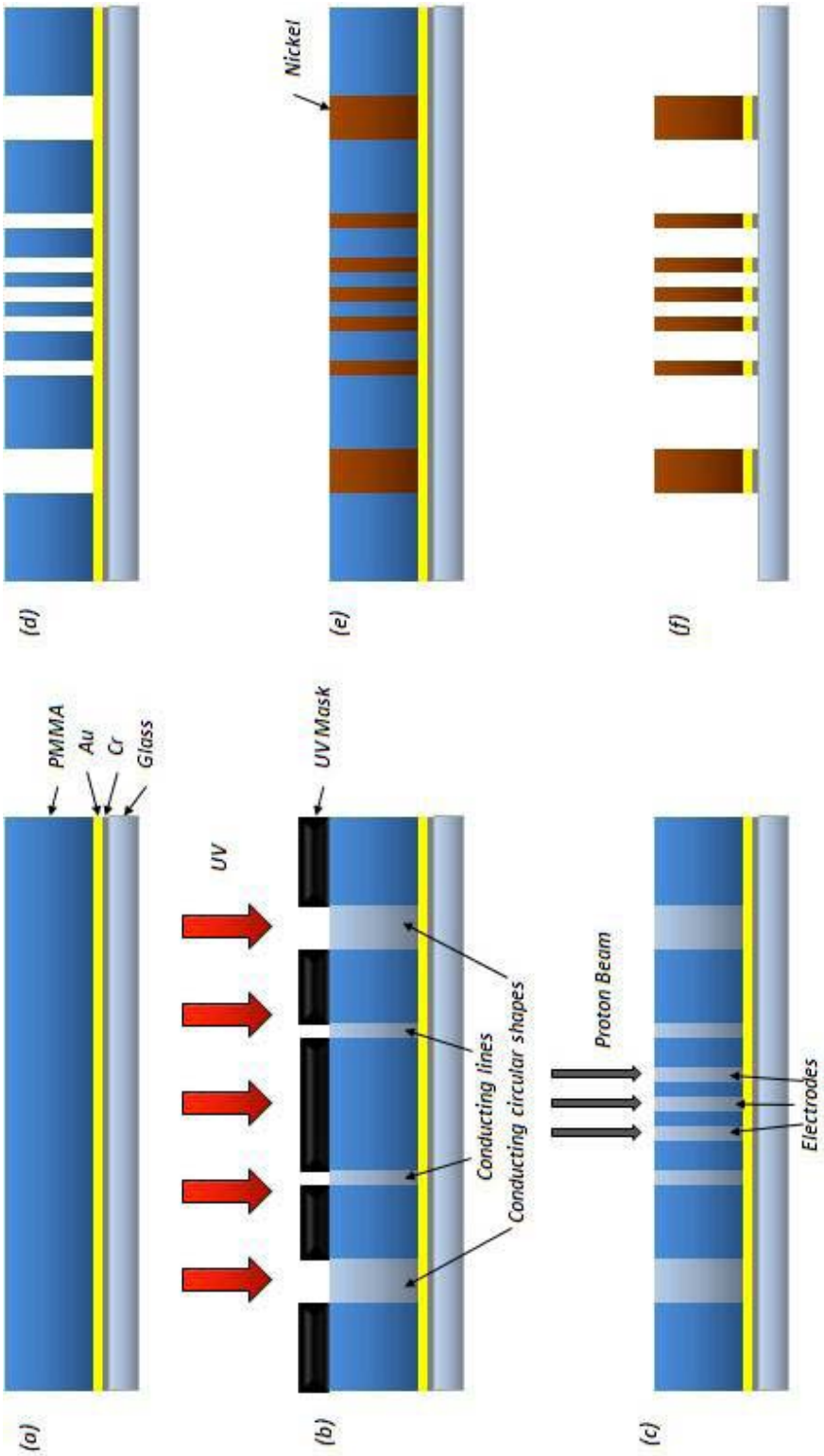

Figure 4.6 Process flow of the biochips fabrication. (a) Cr was sputtered on the glass slip followed by Au for approximately 30 and 10 nm respectively. 7um thick PMMA (495 PMMA A11 resist; solids: 11% in Anisole) is then spin coated on the substrate (b) The circular shapes and the conducting lines are patterned by UV lithography. (c) The electrodes are especially patterned by PBW to achieve straight side walls and high aspect ratio, which cannot be achieved by standard UV lithography. (d) The exposed resist is developed. (e) Nickel is electroplated to form the patterns. (f) The remaining resist and conductive layer are removed.

The last fabrication step is the removal of remaining PMMA and seed layers. The unexposed PMMA resist was removed using Toluene. The sample was placed in the Toluene in 45 ^{o}C hot bath for 1 hour, and rinsed with DI water. After this step, we can observe the nickel electrodes standing on the glass cover slip but with the seed layers still intact. To remove Cr and Au layers, we used Cr and Au etching solutions. The sample was immersed in each solution for 10 seconds, rinsed with DI water, and then gently blown with N_2 gas. Figure 4.5 shows the successfully fabricated biochips for single cell electroporation.

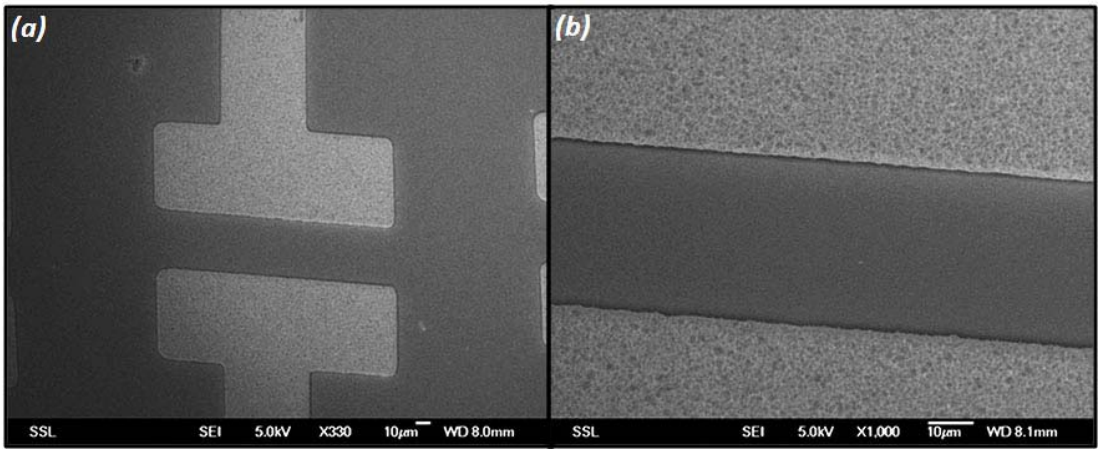

Figure 4.7 SEM pictures of structures on chips fabricated by Proton Beam Writing. The chip was sputtered by Au before the SEM imaging to make the chip conductive (a) one of four pairs of the electrodes in the centre of the chip. Fig (b) was taken in between the gap; top and bottom were ~7 μm-thick Nickel.

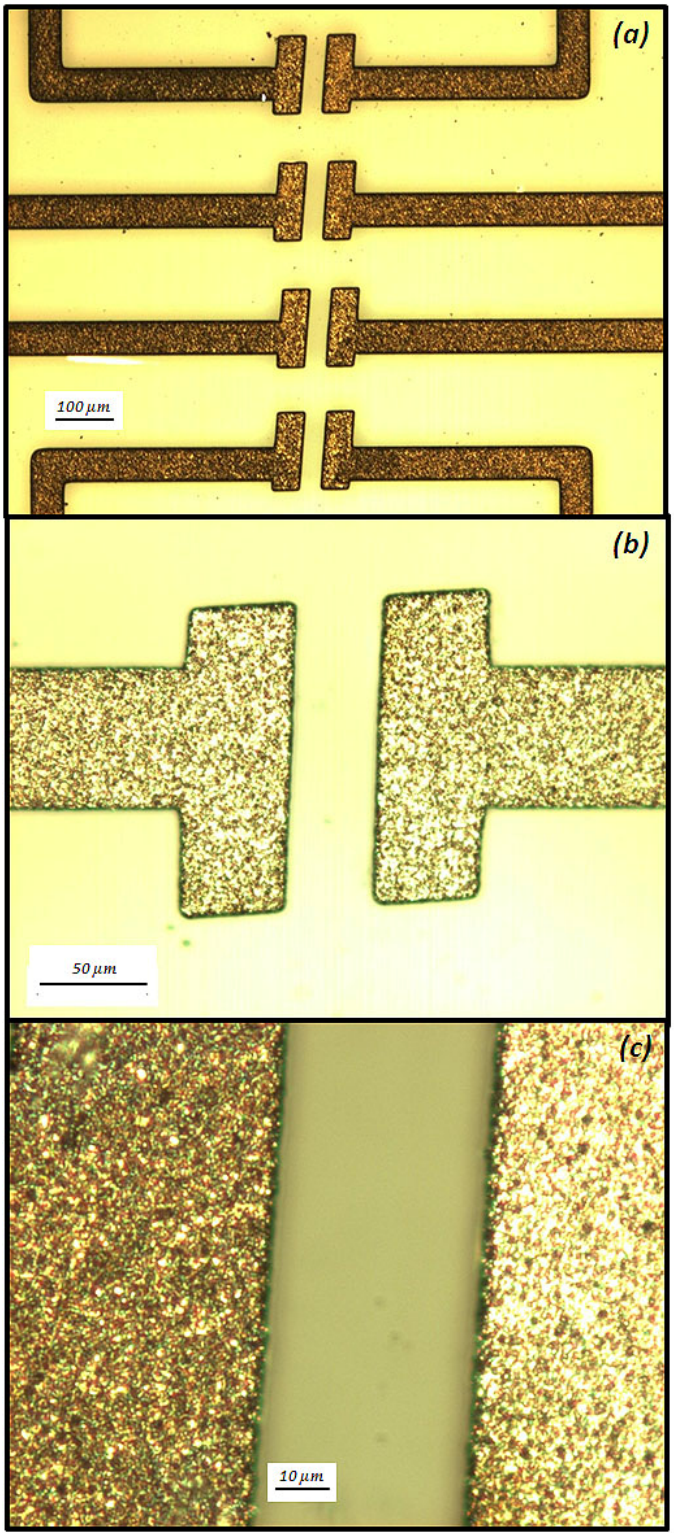

Figure 4.8 Microscope images of structures on chips fabricated by Proton Beam Writing. Fig (a), (b) and (c) were taken with different magnifications (5x, 10x and 20x) showing the structures were electroplated with Nickel.

Using this sequence of steps, the biochips were successfully fabricated. Figure 4.7 and 4.8 show parts of the fabricated electrodes. The SEM images of a pair of electrodes fabricated with proton beam writing are shown in figure 4.7 (a) and (b). The roughness of the side wall is not reported here as it was previously reported by Chiam et al [110] to be 7 nm. Figure 4.8 (a), (b) and (c) are optical images with different magnifications of the final Nickel structures. High spatial resolution is observed for these structures.

4.3 Experimental instruments and methodology

In this section, all the experimental protocols will be explained including cell preparation, cell culture on biochips and the experimental setup for electroporation.

4.3.1 Cell preparation

We used mouse Neuroblastoma N2a cells (ATCC 131, American Type Culture Collection) in the single cell electroporation study. Neuroblastoma cells are used as a model system to study neuronal differentiation, and can be cultured in under standard *in vitro* conditions [118]. The N2a cells were grown in Dulbecco's Modified Eagle's medium (DMEM) supplemented with 25 mM HEPES, 10% fetal bovine serum. All cells were propagated in a humidified incubator at 37 °C with 5% CO_2. The cell recovery and cell passage protocols are described in figure 4.9.

For cell recovery, first the cells were recovered from -150 ^{o}C in a cell culture flask (25 cm^2) filled with 8 mL DMEM at 37 ^{o}C. After 24 hours, the medium was changed and the cells continued to be recovered for another 48 hours. At this stage the culture flask bottom surface should be at least 80-90% covered with the healthy cells, which indicates that the cell recovery is successful. After 48-72 hours, the cells have to be passaged in order to maintain the healthy condition. The cell passage protocol is described as following steps:

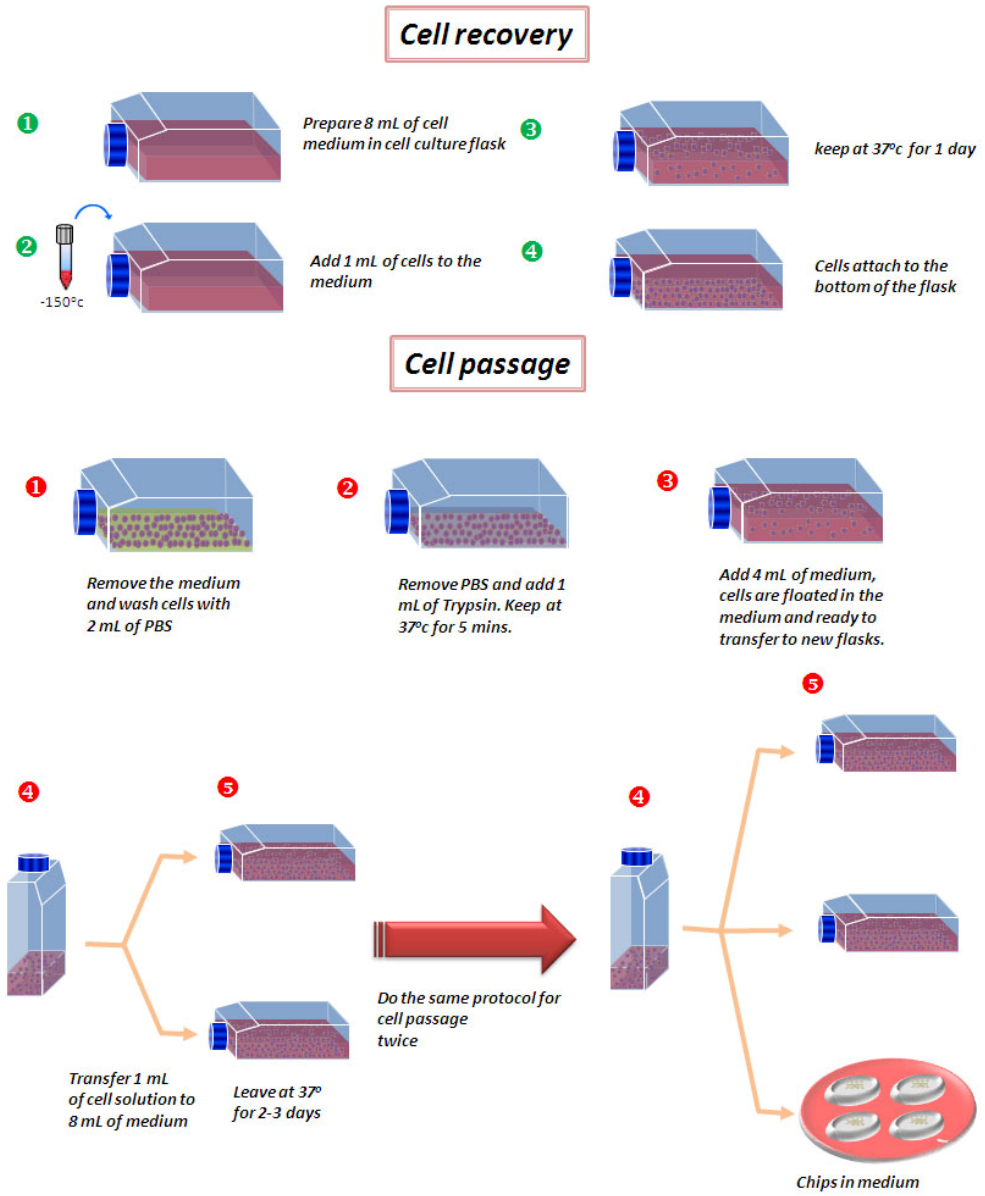

Figure 4.9 Cell recovery and cell passage protocols. The cell recovery is the method for recovering the cells from being suspended at very low temperature (-150°C). The frozen cells were immediately added into the fresh cell culture medium when they melted. The successfully recovered cells from this step will attach to the bottom of the culture flask. The second protocol is cell passage. This protocol is for keeping cells alive. The protocol is normally repeated every 3 to 4 days. The cells are usually passed to the biochips at the last step of this protocol.

(a) Remove the old medium in the flask and add 5 mL PBS; gently shake and remove. Then add 1 mL of 1X Tripsin and incubate at 37^{o}C for 5 minutes to detach the cells from the flask surface.

(b) Add 4 mL of cell culture medium to the same flask; shake to detach all the cells from the bottom of the flask to the solution.

(c) Take out all 5 mL of cell solution to 15 mL tube and tab or shake the tube to isolate the cells.

(d) Add 600 μL of isolated cell solution to a new flask with 8 mL cell culture medium, and incubate at 37 ^{o}C for 3-4 days until the bottom is 80-90 % covered.

Once the cells fully cover the bottom of the flask, a cell passage protocol must be taken place. The cell passaging is a technique that keeps the cells alive and growing under cultured conditions for extended periods of time. All cells should be passaged every 2-4 days before they become confluent i.e. no more space available in the culture flask surface. After the cell passage has performed at least twice, the cells should be fully recovered and healthy for growing onto the electroporation biochips. To grow the cells on the biochips, we followed the same cell passaging protocol, and used the same cell solution used for normal passage for the chips. The chips and cell culture dishes (35 mm x 10 mm) are exposed under UV light for 20 minutes (both sides for biochips) for sterilization before 500 μL of cell solution is added on 2 mL of fresh cell medium inside the culture dish. After the cells are grown inside the incubator for approximately 72 hours, the cells should be attached on the chip surface and will be ready for the electroporation experiments.

The successfully grown cells adhering to the biochip surface are shown in figure 4.10. The healthy cells normally cover the whole surface of the cover slip including the areas between the electrode gaps.

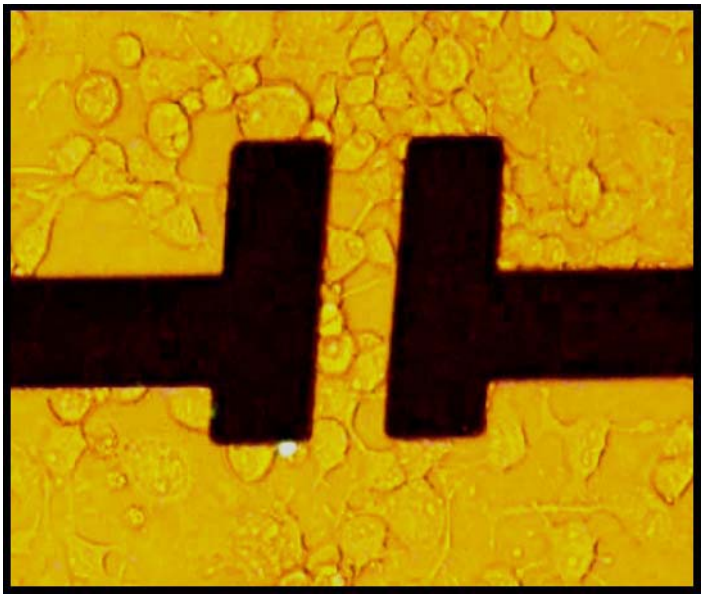

Figure 4.10 Neuroblastoma cells are grown in between the electrodes ready for electroporation. The cells are incubated at 37 ^{o}C for 72 hours.

4.3.2 Fluorescent stains

The efficacy of fluorescent compounds as labels for membrane- compromised cells is governed by their selectivity, brightness, excitation and emission maxima, and inherent biological toxicity. Ideal indicators of plasma membrane integrity concentrate only in cells with permeabilized membranes and exhibit marked fluorescence enhancement within these cells[119]. DNA and RNA provide large numbers of intracellular binding sites that promote marked fluorescence enhancement of many different stains. The phenanthridium nucleic acid stains such as ethidium bromide, propidium iodide, and ethidium homodimer 1 and 2 have been used almost exclusively to evaluate the integrity of the plasma membrane by fluorescence in a variety of animal cells and bacterial species [120-124]. SYTOX Green stain provides several important advantages over these compounds, making it a preferred candidate for a variety of fluorescence- based applications in microbiology [125]. Therefore, we decided to use SYTOX green for our experiments.

SYTOX® Green nucleic acid stain (S-7020, Invitrogen) is a high-affinity nucleic acid stain that easily penetrates cells with compromised plasma membranes and yet will not cross the membranes of live cells. This characteristic makes the stain very suitable for electroporation because if the cells will allow the stain to pass through after they are electroporated, and they can be observed under fluorescent microscope. The SYTOX® Green is characterized by a high quantum yield and fluorescence enhancement upon binding to nucleic acids, with excitation and emission maxima of about 505 and 525 nm, respectively.

The SYTOX® Green dye is supplied as a 5 mM solution in dimethylsulfoxide (DMSO); the DMSO solution may be subjected to many freeze-thaw cycles without reagent degradation. We prepared the stock of 500 nM SYTOX® Green in PBS. Before the electroporation experiment, 20 μL of the stock was added to the chip which was covered with 2 mL Borate Saline Solution (BSS) buffer; the concentration of the stain then became 0.5 nM. This concentration gives very high brightness of the stained cells and easier observed under fluorescence microscope. Figure 4.11 (a) shows the microscope image of dead N2a cells stained with SYTOX® Green. As electroporation buffer, we used BSS (pH 7.4 adjusted with HEPES) because it is suitable for mammalian cell types. The pH is also important where in general it should mimic the composition of the cytoplasm of the cell[35]. The pH of our buffer is closely aligned to the usual intracellular pH.

For testing the cell viability after electroporation, we used another dye called Ethidium homodimer II (EthD-2). The EthD-2 is a high affinity fluorescent nucleic acid stain. It binds to both DNA and RNA in a sequence-independent manner and with a >30-fold fluorescence enhancement. The dye is highly positive charged and, similar to SYTOX® Green, it cannot cross cell membranes to stain living cells. The dye is soluble in water and has excitation and emission wavelengths of about 535 and 624 nm, respectively. The stock was prepared at 50 nM in PBS. The same protocol as SYTOX® Green was used after the electroporation. The cells are stained for 30 minutes before observing under microscope. Figure 4.11 show the fluorescent images of cells in the same position. Only dead cells give bright fluorescence in both colours. Figure 4.11 (a) was taken using bright field to see the entire cells on the surface. Figure 4.11 (b) and (c)

are dark field images taken by microscope. The cells were excited using halogen lamp with blue and green colour filters to excite SYTOX® Green and EthD-2, respectively. It can also be seen from figure 4.11 (a) that the dead and live cells look different in the morphological appearance under microscope.

The protocol therefore is to use the two stains to differentiate which cells have been electroporated but recover and remain viable, with those which have died during the electroporation process.

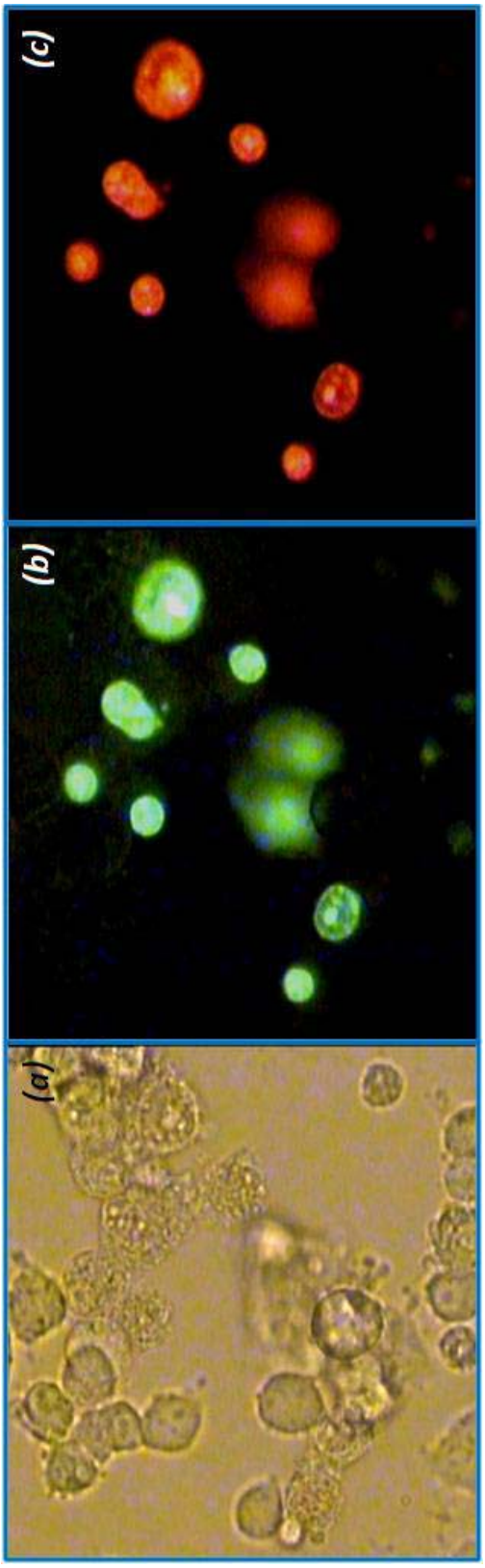

Figure 4.11 Stained dead N2a cells with SYTOX® Green and Ethidium homodimer II. (a) Bright field microscope image of live and dead cells. (b) Dark field image with halogen lamp incorporated with the blue filter. The dead cells stained with SYTOX® Green are excited and fluoresce in green color. (c) Dark field image with halogen lamp incorporated with the green filter. The dead cell stained with Ethidium homodimer II are excited and fluoresce in red color. Live cells do not fluoresce in both colors.

4.3.3 Experimental setup and method

The setup for electroporation is shown in figure 4.12 (a). The overall system consists of a pulse generator (AV-1010-B, Avtech Electrosystems Ltd.), an inverted microscope (Eclipse TE2000-U, Nikon), 3D manipulators, a 3D stage controller and a computer (not shown in the figure) for controlling the pulse generator and collecting data. The 3D manipulators were utilized to control and move the small tip probes from the pulse generator which were placed in contact with the conducting circular pads. The pulses were generated by the pulse generator which was in turn controlled by a computer program. From the program, we were able to control and change parameters of pulse, i.e. pulse amplitude, number of pulses and pulse duration. The generated pulses were applied via the probes and the conducting pads, to the electrodes between which the cells were attached. . The chip was monitored using a camera in real time attached to the inverted microscope.

In order to investigate whether electroporation of N2a can offer a potential competitive advantage over conventional methods, the electrical parameters affecting the effectiveness of the process needs to be optimized. Pulse amplitudes between 3.75 V and 5.00 V across the 50 μm gap, the number of successive pulses from 1 to 10, and the pulse duration between 0.5 and 6.0 ms were tested on cell viability and permeabilization. We used square wave pulses for all the experiments because they appear to provide in vitro experimental conditions resulting in levels of cell survival that cannot be reached using exponentially decaying pulses. [97]

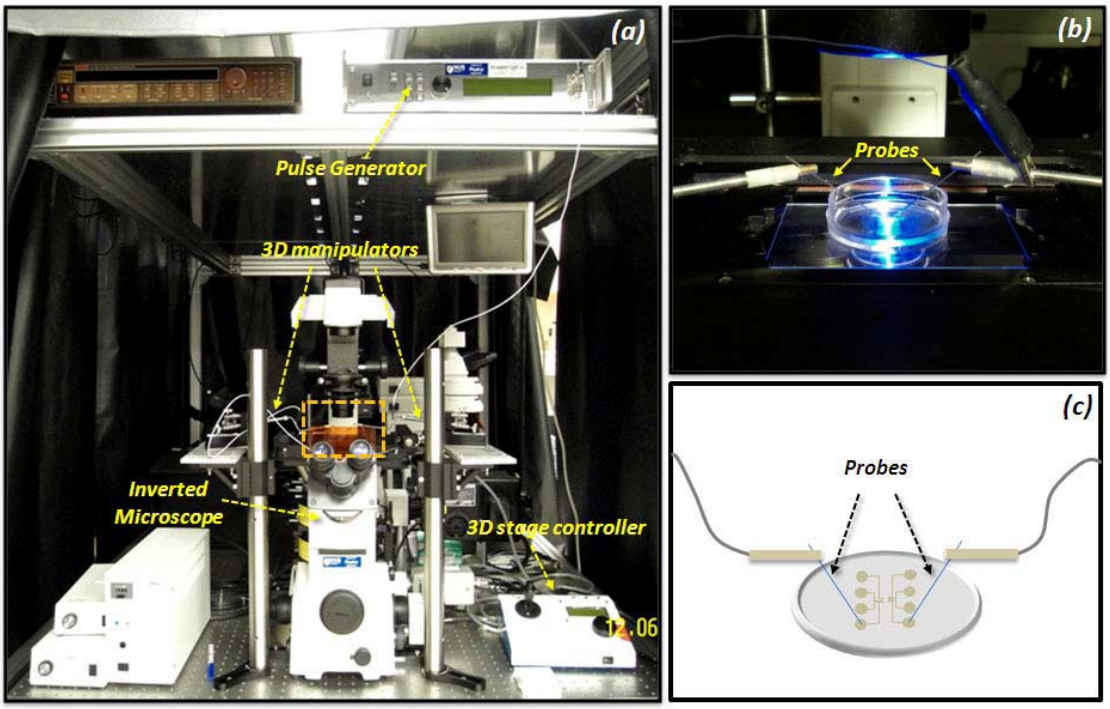

Figure 4.12 Experimental Setup. (a) The overall system consists of the pulse generator, inverted microscope, 3D manipulators and 3D stage controller. (b) The chip is monitored and performed the experiments on the microscope stage. With the connected camera, the videos and images can be captured while doing the experiments. (c) The schematic representation of the chip while performing the experiment. The small probe tips are connected to a pair of the electrode before the pulses are given and passed through the centre of the chip where there were cells in between the chosen electrode gap.

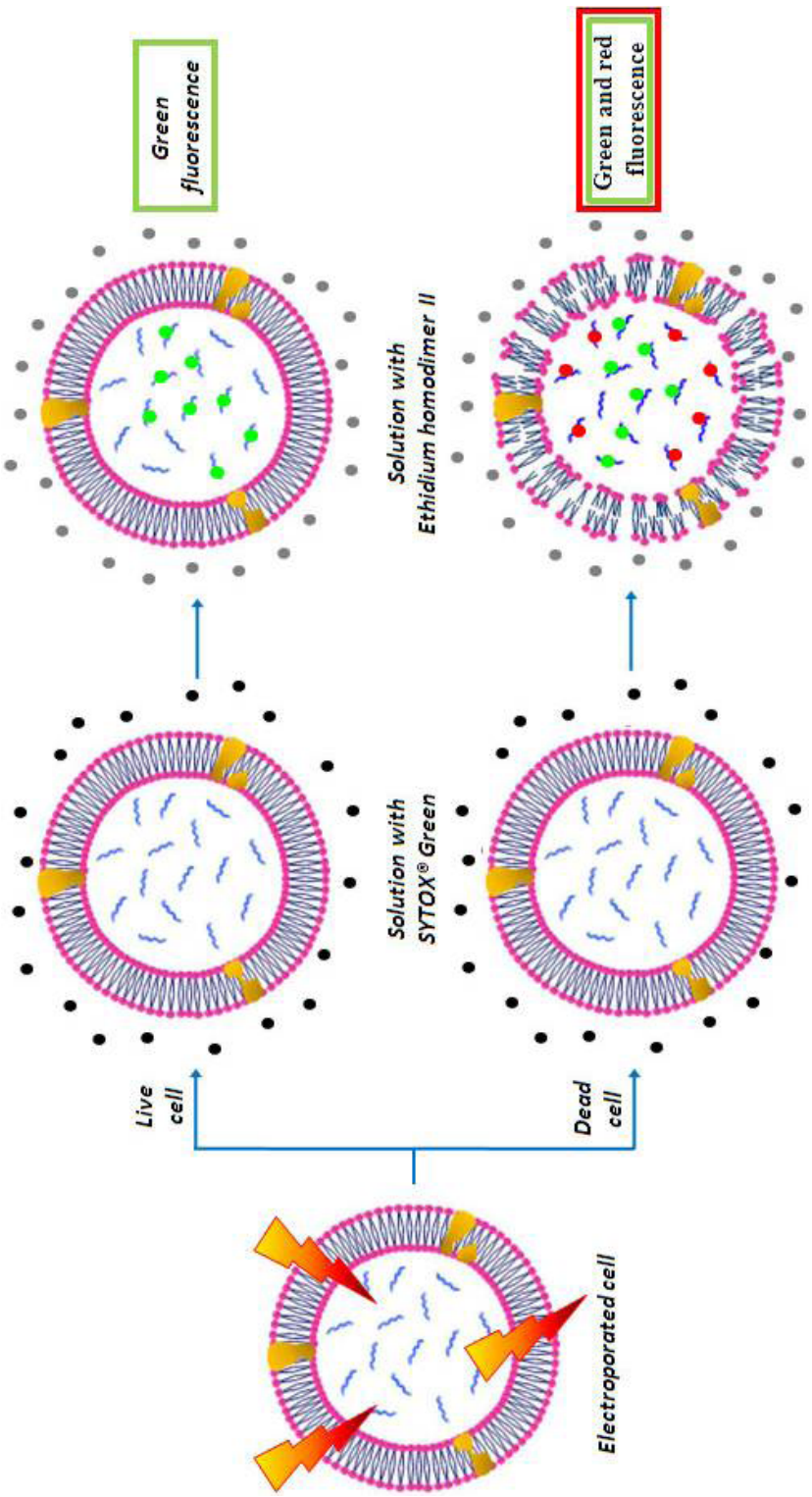

Figure 4.13 Illustration the utilization of SYTOX® Green and Ethidium homodimer II to determine electroporated and dead cells. The SYTOX® Green was added in the solution before the electroporation was performed; both electroporated and dead cells were stained with this dye. The Ethidium homodimer II, added 30 minutes after electroporation, was used for testing viability of cells; only dead cells were stained with this dye. This results in 2-colour fluorescence in dead cells.

Two sets of experiments were performed to obtain the percentage of electropermeabilized cells (figure 4.13). In the first experiment, 20 μL of 500 nM SYTOX® Green stain was added to the cells attached between the electrodes, before electroporation. These cells were then processed by the biochips under varying electrical parameters (pulse amplitude, number of pulses and pulse duration) and the fluorescent and non-fluorescent cells were imaged and counted. In the second experiment, 20 μL of 50 nM DEAD Red™ (commercial name of Ethidium homodimer II) was added 30 minutes after electroporation was performed to stain the dead cells The cells will fluoresce when excited by a halogen lamp if the stains are successfully bound to the DNA. Green florescence hence serves as an indication that the cells have been successfully electroporated while subsequent red fluorescence indicates that the cells died during the electroporation.

4.4 Results and discussion

In this section, we report the results of the biochip fabrication and the optimization of pulse parameters; pulse amplitude, number of pulses and pulse duration using our novel biochips for single cell electroporation.

Single-cell electroporation and pulse parameter optimization

The electroporation for single N2a cells was performed. Preliminary experiment showed the successful cell transfection. After pulses were given, the cells positioned between a pair of electrode gradually emitted green fluorescence when excited with halogen lamp and blue filter.

The electroporated cells on our biochips were in a healthier condition than those in the conventional cuvette system because they did not have to be suspended in any medium before electroporation. The electroporation results were extracted from the optical images taken from inverted microscope. The transfection rate and the viability are given by:

$$Transfection\ rate(\%) = \frac{Total\ number\ of\ electroporated\ cells}{Total\ number\ of\ live\ cells\ (before\ electroporation)} \times 100$$

$$Viability\ rate(\%) = \frac{Total\ number\ of\ live\ cells\ (after\ electroporation) - Total\ number\ of\ dead\ cells}{Total\ number\ of\ live\ cells\ (after\ electroporation)} \times 100$$

Figure 4.14 shows examples of successfully transfected cells. Figure 4.14(a) shows images of cells in between the electrodes before electroporation was performed. Both Figure 4.14 (b) and (c) were taken from the same electrode pair, with different filters (different excitation wavelengths), while Figure 4.14 (b) was taken 30 minutes after the electroporation, and Figure 4.14 (c) was taken 30 minutes later after the buffer with SYTOX® Green was removed, and the chips were incubated with DEAD Red™. The figures showed that more cells fluoresce in green than in green and red. The cells indicated with yellow arrows still survive after electroporation.

The crucial factor for successful electropermeabilization of living cells is the choice of appropriate field strength. As mentioned in chapter 2, the electric field strength delivered must reach a threshold value that result in a change in transmembrane potential. However, the electric field strength should remain below values leading to permanent irreversible damage to cell membrane structure. Here, we optimized 3 most important pulse parameters: pulse amplitude, number of pulses and pulse duration. The square-

wave pulses were used for all the experiments as they are more efficient than exponential decay pulses. According to Lin et al.[85], they have studied the electroporation in microchips using 10 pulses with pulse duration from 1 to 20 ms. Therefore, the first parameter we optimized was pulse amplitude with fixed number of pulses (10 pulses) and pulse duration (4 ms). The pulse amplitudes were varied from 3.75 to 5.00 volts across 5-μm gap.

The results for optimal electroporation conditions were shown in Figure 4.15. For pulse amplitude optimization, the experiments were performed with various pulse amplitude (3.75, 4.00, 4.25, 4.50, 4.75 and 5.00 volts across 50-micron gap) while number of pulses and pulse duration were fixed at 10 pulses, and 4 ms, respectively (figure 4.15(a)). We have collected the data 5 times per data point, and the error bars are from the standard deviation of all 5 values collected from each point. The standard deviation is a statistical measure of spread or variability; it is the root mean square (RMS) deviation of the value from their arithmetic mean. The standard deviation can be calculated using equation (4.15)

$$Standard\ Deviation\ (\sigma) = \sqrt{\frac{1}{N}\sum_{i=1}^{N}(x_i - \bar{x})^2} \qquad (4.15)$$

Where N is the sample size or number of collected data (scores),

x is the individual score and

$\bar{x}$ is the mean of the score

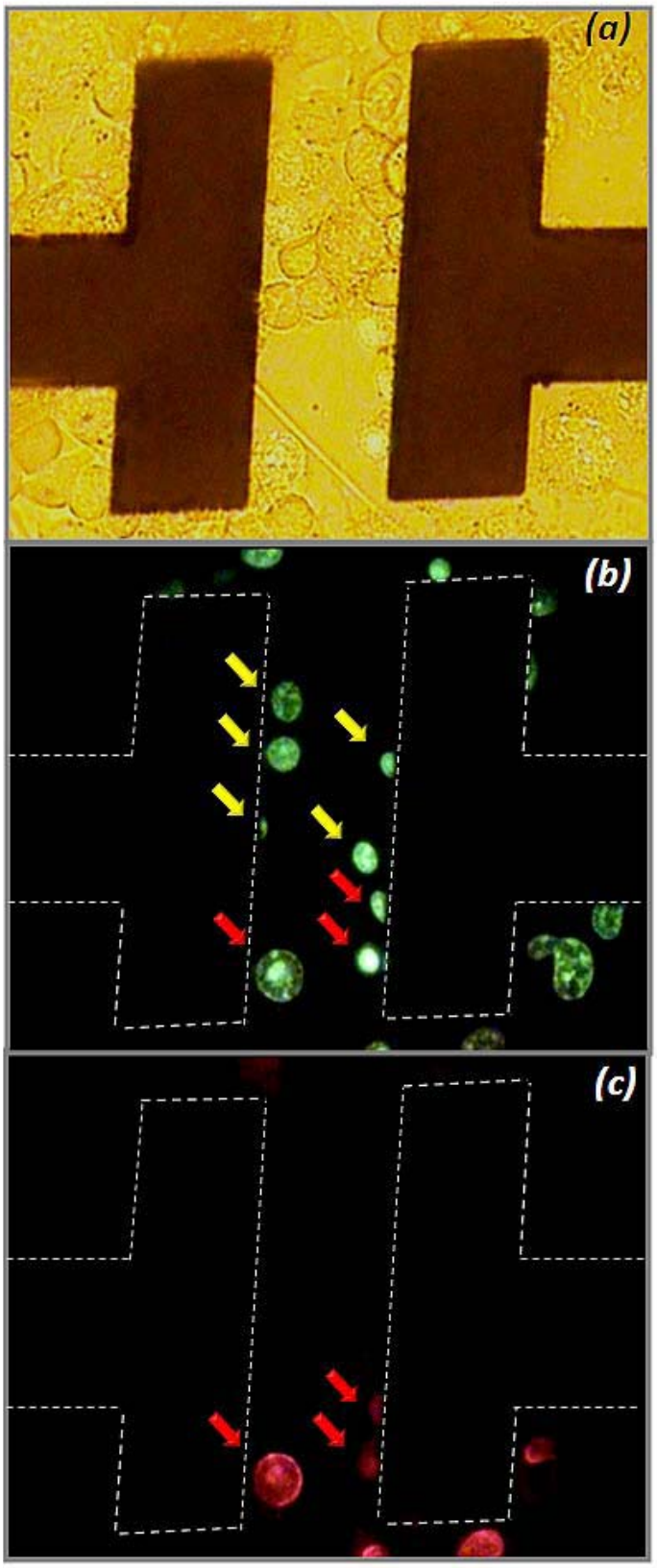

Figure 4.14 Example result from one electroporation experiment. Optical images have been taken using an inverted microscope with 20X magnification. (a) Cells are successfully grown in between a pair of electrode gap before the experiment. (b) Fluorescent image of cells shows green-fluorescent cells which uptook SYTOX® Green and (c) fluorescent image of cells shows red-fluorescent cells which uptook DEAD Red™. (b) and (c) were taken after cells were electroporated with 10 4.25-Volt electric pulses.

The results from the pulse amplitude optimization showed that the highest percentage of cell viability was obtained at 4.25 volts, and a very high electroporation rate was also achieved. It was found from previous work that the typical transmembrane potential is in the range of 0.2-1 volt mainly depending on size of the cells [126]. Since N2A cells are about 10μm, and the optimum pulse amplitude is 4.25 volts in 50 micrometers, the potential across N2A cells is ~0.85 volt which is in agreement with the theory.

Figure 4.15 (b) shows an optimization of number of pulses when the pulse amplitude and pulse duration were fixed at 4.25 V and 4 ms respectively. We have also collected the data 5 times per data point, and the error bars are from the standard deviation of all 5 values collected from each point. The results showed that 4 pulses gave the highest percentage of transfection and cell viability at 78.2 and 78.3 percent respectively. Figure 4.15 (c) shows an optimization of pulse duration when the pulse amplitude and pulse duration were fixed at 4.25 V and 4 pulses respectively. Each data point was extracted from 3 collected values and the error bars show the standard deviation of the values. The results showed that 2-ms pulse gave the highest percentage of transfection rate at 82.1 percent.

Compared to previous works, Guignet and Meyer [127] have studied suspended-drop electroporation on differentiated human promyelocytic leukemia cells, 3T3-L1 adipocytes and RBL-2H3 tumor mast cells was presented transfection efficiency and viability rate of 45-65% and 40-60%, respectively. The other work from Hung et al. was reported up to 62% transfection rate of the electroporation biochip to deliver typan-blue dye into zebrafish embryos. Also compared to the conventional electroporation

techniques which have a transfection rate of 20-50 percent, we have achieved better efficiency with our biochip design.

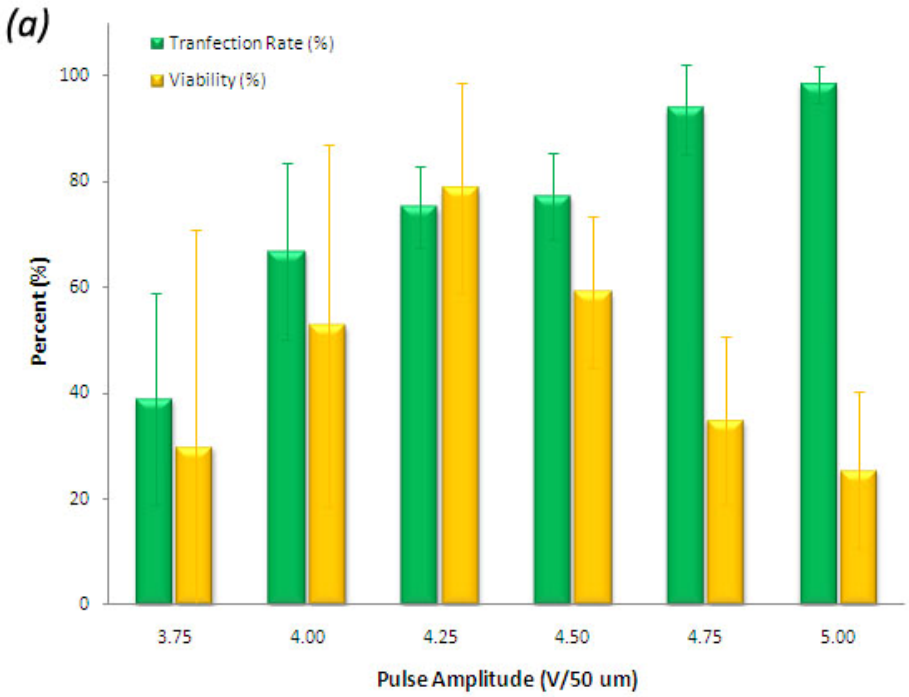

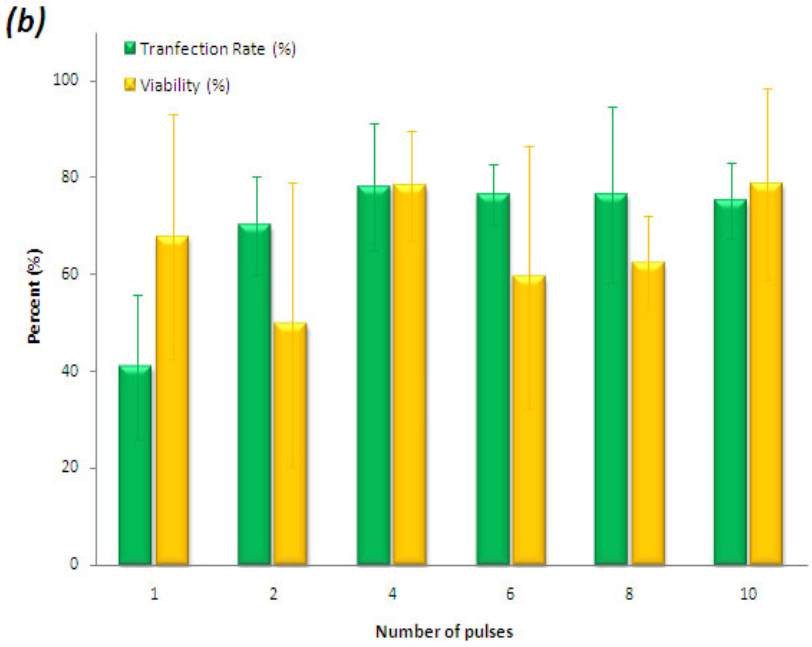

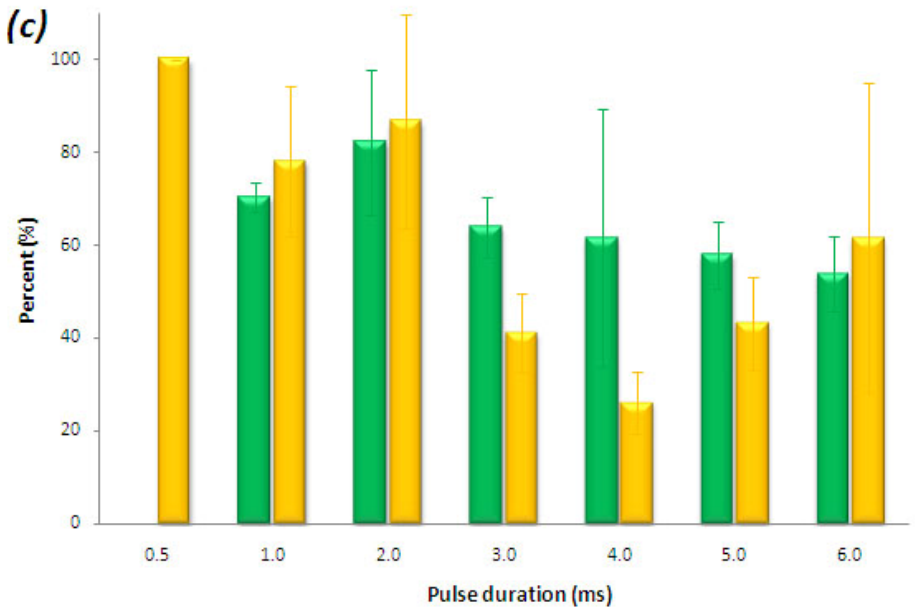

Figure 4.15 Pulse parameter optimization. (a) Pulse amplitude optimization (3.75, 4.00, 4.25, 4.50, 4.75 and 5.00 V/50μm with 4 ms 10 pulses). The optimized pulse amplitude is at 4.25 V/50μm (equal to 0.85 kV/cm^{-1}), it gives highest cell viability and very good transfection rate. (b) Number of pulses optimization (1, 2, 4, 6, 8 and 10 pulses with 4 ms- 4.25 V/50μm pulse). 4 pulses give very high in both transfection and viability rates. (c) Pulse duration optimization (0.5, 1.0, 2.0, 3.0, 4.0, 5.0 and 6.0 ms with 4 of 4.25 V/50μm pulses). 2 ms pulse gives highest transfection rate at 82.1 %, and viability rate at 86.7%.

4.5 Conclusion.

A novel electroporation micro-biochip was successfully fabricated. Each pair of electrodes is spaced 50 μm apart, much smaller than the conventional electroporator. These gaps give larger and more uniform electric field distributions which benefits the electroporation process. The unprecedented usage of PBW technique in the fabrication processes to achieve electrodes with high aspect-ratio and straight side walls was also demonstrated. In addition, in tests we observed that these biochips can be reused up to 24 times before deteriorating.

In our study, the optimal parameters for successful electroporation of N2a cells were reached. A range of the pulse amplitudes, the number of pulses, and the pulse duration were tested, revealing that the appropriate combination would be 0.85 kV/cm^{-1}, 2 ms of 4 square electric pulses.

Detailed studies on the effects of the pulse amplitudes, the number of pulses, and the pulse duration were carried out and optimized. High transfection rate of 82.1% and survival rate of 86.7% were achieved, higher than most conventional electroporators and previously reported microelectroporators. This result demonstrated that our biochip is an efficient tool to introduce impermeant materials, such as drugs, DNA and protein, into individual cells. We were also the first to demonstrate single-cell electroporation in Mouse Neuroblastoma (N2a) cells. Since neuroblastoma cells are used as a model system to study neuronal differentiation [128], our work could pave the way for the studies of regulation of neural cell development. Nevertheless, this work is still in its early stages. Parameters such as an oxidization of the electrodes, temperature, buffer composition and

wave forms have to be studied and optimized so that higher transfection rate and viability rate may be achieved.

Chapter 5

Cell Fluorescence Imaging

There has been a remarkable growth in the use of fluorescence imaging in the biological sciences during the past 20 years. Fluorescence spectroscopy is considered to be one of the leading research tools in biochemistry and biophysics. However, the spatial resolution of conventional optical fluorescence microscopy is limited by the diffraction limit of light at ~250 nm. In this chapter, we report the new technique for fluorescence imaging using a proton beam. With our novel Proton Beam Writing (PBW) facility at CIBA we have the ability to focus the beam down to less than 100 nm of the spot size, and because of this we can fabricate 3D structures below the 100nm level. This is achieved due to the physical properties of the fast proton, having high penetrating properties, straight line trajectories, and minimal proximity effects (absence of long range secondary electrons). However, using the same physical properties, it should be possible to image fluorescence stained biological cells with higher resolution and contrast compared with other conventional methods. Ultimately Proton Induced Fluorescence (PIF) has better resolutions than conventional confocal or optical fluorescence due to the superior physical properties of the proton. In this chapter, PIF images and Proton Induced Secondary Electron (PISE) images of normal and electroporated cells from our novel electroporation biochip are reported.

Introduction

The same physical properties that enable protons to fabricate 3D structures at high resolutions and high aspect ratio, also allow high spatial resolution microscopy of thick samples. Udalagama et al.[129] have investigated the energy-deposition features of both primary MeV protons and keV electrons interaction with matter with reference to proton beam writing. Their calculations however are equally valid for fluorescence microscopy, where the lateral range of secondary electrons plays an important role in the ultimate resolutions achievable. They have shown that protons are able to maintain spatial compactness of their spatial energy-deposition profiles (SEDPs) at sample depths much greater than for electrons. Figure 5.1 shows the radial deposition for 2 MeV protons (5.1(a)) and 100 keV electrons (5.1(b)) in 5-μm-thick PMMA resist. Electron penetration was characterized by a rapid broadening of the SEDPs with depth thereby leading to significant, so-called, proximity effects (unintended exposure of unirradiated regions of the sample) that present problems in electron-beam lithography.

As predicted by the Born approximation, the z^2/v^2 scaling of energy loss implies that an electron must have approx 1850 times less energy than a proton to display an equivalent rate of energy loss. Therefore the energy deposition characteristics of 2 MeV protons used in PBW will be similar to 1 keV electrons. However, such low-electron energies however are currently of little practical interest in electron-beam lithography, where 10–100 keV electron energies are used.

By using Monte Carlo calculation, Udalagama et al. also showed that the secondary electrons (δ rays) produced by penetrating protons have a much reduced spatial energy

spread compared with those generated from primary electrons, thereby minimizing ion-proximity effects in comparison to electrons. Therefore, the potential for using protons for nanostructuring and nanoprobing down to the nanometre level is very promising.

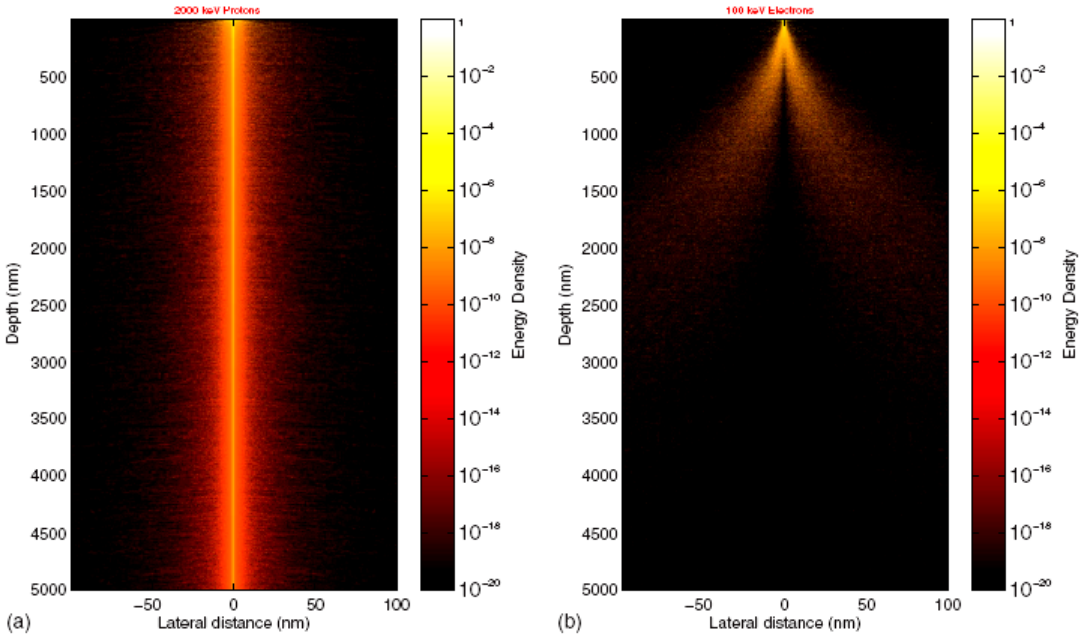

Figure 5.1 Simulation of the radial deposition of energy for 2 MeV protons (left) and 100 keV electrons (right) for a 5- μm-thick layer of PMMA.

If the stochastic ion-matter interactions allow a well-focused proton beam to retain its spatial compactness at the nanometer scale then this opens up numerous possibilities for the use of MeV protons. For instance, MeV protons can be used to induce fluorescence, enabling high spatial-resolution fluorescence imaging of thick samples such as whole biological cells. This will complement existing confocal or optical fluorescence microscopies, which are diffraction limited to around 200 nm spatial resolutions.

5.1 Introduction to fluorescence microscopy

Fluorescence microscopy has become an essential tool in biology and the biomedical sciences, as well as in material science. This section is an introduction to fluorescence and fluorescence microscopy.

5.1.1 Principles of fluorescence

Fluorescence is the property of some atoms and molecules to absorb light of a particular wavelength and after a brief interval, termed the *fluorescence lifetime* that is normally in nanoseconds, to emit light at longer wavelengths. It is proportional to the amount of light absorbed × quantum yield. For low optical densities, Beer's law states that the amount of fluorescence is proportional to the product of the light absorbed ($I_0\varepsilon[c]x$) by the fluorophore and the quantum yield, Q:

$$F = I_0\varepsilon[c]xQ \tag{5.1}$$

Where I_0 is the intensity of the light beam falling on the solution ,

ε is the molar extinction coefficient of the fluorophore,

c is the concentration of the fluorophore and

x is the pathlength through the solution.

Fundamentals of Excitation and Emission

Fluorescence is one of the ubiquitous luminescence family of processes in which affected molecules emit light from electronically excited states created by either a physical (i.e. absorption of light or charged particles), mechanical (friction), or chemical mechanism. Generation of luminescence through excitation of a molecule by photons (UV or visible light) is a phenomenon termed *photoluminescence*, which is formally divided into two categories, *fluorescence* and *phosphorescence*, depending upon the electronic configuration of the excited state and the emission pathway. The process of phosphorescence occurs in a manner similar to fluorescence, but with a much longer excited state lifetime.

Absorption of energy by fluorophores (a component of a molecule that causes that molecule to be fluorescent) occurs between the closely spaced vibrational and rotational energy levels of the excited states in different molecular orbitals. The various energy levels involved in the absorption and emission of light by a fluorophore are classically presented by a Jablonski energy diagram (see figure 5.2), named in honor of the Polish physicist Professor Alexander Jablonski.

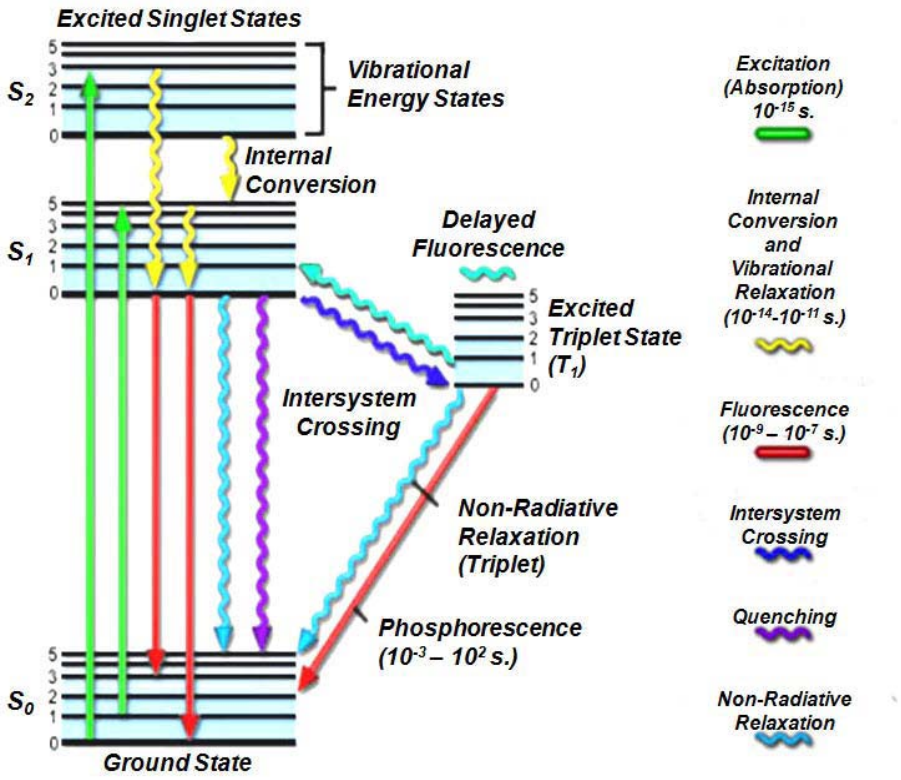

Figure 5.2 Illustration of one form of a Jablonski diagram. The singlet ground (S(0)) state, as well as the first (S(1)) and second (S(2)) excited singlet states as a stack of horizontal lines. The thicker lines represent electronic energy levels, while the thinner lines denote the various vibrational energy states (rotational energy states are ignored). Transitions between the states are illustrated as straight or wavy arrows, depending upon whether the transition is associated with absorption or emission of a photon (straight arrow) or results from a molecular internal conversion or non-radiative relaxation process (wavy arrows). Vertical upward arrows are utilized to indicate the instantaneous nature of excitation processes, while the wavy arrows are reserved for those events that occur on a much longer timescale.

Absorption of light occurs very quickly (approximately a femtosecond, the time necessary for the photon to travel a single wavelength) in discrete amounts termed *quanta* and corresponds to excitation of the fluorophore from the ground state to an excited state. The energy in a quantum (Planck's Law) is expressed by the equation:

$$E = h\nu = \frac{hc}{\lambda} \tag{5.2}$$

where E is the energy,

h is Planck's constant,

ν and λ are the frequency and wavelength of the incoming photon, and

c is the speed of light.

Planck's Law states that the radiation energy of an absorbed photon is directly proportional to the frequency and inversely proportional to the wavelength. In other words, shorter incident wavelengths possess a greater quantum of energy. The absorption of a photon of energy by a fluorophore, which occurs due to an interaction of the oscillating electric field vector of the light wave with charges (electrons) in the molecule, is an all or none phenomenon and can only occur with incident light of specific wavelengths known as *absorption bands*. If the absorbed photon contains more energy than is necessary for a simple electronic transition, the excess energy is usually converted into vibrational and rotational energy. However, if a collision occurs between a molecule and a photon having insufficient energy to promote a transition, no absorption occurs. The spectrally broad absorption band arises from the closely spaced vibrational energy levels plus thermal motion that enables a range of photon energies to match a particular transition. Because excitation of a molecule by absorption normally occurs without a

change in electron spin-pairing, the excited state is also a singlet. In general, fluorescence investigations are conducted with radiation having wavelengths ranging from the ultraviolet to the visible regions of the electromagnetic spectrum (250 to 700 nanometers).

With ultraviolet or visible light, common fluorophores are usually excited to higher vibrational levels of the first (*S(1)*) or second (*S(2)*) singlet energy state. Two of the absorption (or excitation) transitions presented in figure 5.1 (left-hand green arrows) occurs from the low vibrational energy level of the ground state to a higher vibrational level in the first and second excited states (a transition denoted as *S(0)* = 0 to *S(2)* = 3 and as *S(0)* = 1 to *S(1)* = 5). In a typical fluorophore, irradiation with a wide spectrum of wavelengths will generate an entire range of allowed transitions that populate the various vibrational energy levels of the excited states. Some of these transitions will have a much higher degree of probability than others, and when combined, will constitute the absorption spectrum of the molecule. Note that for most fluorophores, the absorption and excitation spectra are distinct, but often overlap and can sometimes become indistinguishable. In other cases (fluorescein, for example) the absorption and excitation spectra are clearly separated.

Fluorescence is normally observed as emission intensity over a band of wavelengths rather than a sharp line. Most fluorophores can repeat the excitation and emission cycle many hundreds to thousands of times before the highly reactive excited state molecule is *photobleached*, resulting in the destruction of fluorescence.

Table 1 Timescale Range for Fluorescence Processes

Transition	*Process*	*Rate Constant*	*Timescale (Seconds)*
S(0) => S(1) or S(n)	*Absorption (Excitation)*	*Instantaneous*	10^{-15}
S(n) => S(1)	*Internal Conversion*	*k(ic)*	10^{-14} to 10^{-10}
S(1) => S(1)	*Vibrational Relaxation*	*k(vr)*	10^{-12} to 10^{-10}
S(1) => S(0)	*Fluorescence*	*k(f) or G*	10^{-9} to 10^{-7}
S(1) => T(1)	*Intersystem Crossing*	*k(pT)*	10^{-10} to 10^{-8}
S(1) => S(0)	*Non-Radiative Relaxation Quenching*	*k(nr), k(q)*	10^{-7} to 10^{-5}
T(1) => S(0)	*Phosphorescence*	*k(p)*	10^{-3} to 100
T(1) => S(0)	*Non-Radiative Relaxation Quenching*	*k(nr), k(qT)*	10^{-3} to 100

The fluorescence process is governed by three important events: excitation, relaxation and emission, all of which occur on timescales that are separated by several orders of magnitude (see Table 1). The excitation of a susceptible molecule by an incoming photon happens in femtoseconds (10^{-15} seconds), while the vibrational relaxation of excited state electrons to the lowest energy level is much slower and can be measured in picoseconds (10^{-12} seconds). The final process, the emission of a longer wavelength photon and return of the molecule to the ground state, occurs in the relatively long time period of nanoseconds (10^{-9} seconds). Although the entire molecular fluorescence lifetime, from excitation to emission, is measured in only billionths of a second, the phenomenon is a stunning manifestation of the interaction between light and matter that forms the basis for the expansive fields of steady state and time-resolved fluorescence spectroscopy and microscopy. Because of the tremendously sensitive

emission profiles, spatial resolution, and high specificity of fluorescence investigations, the technique is rapidly becoming an important tool in genetics and cell biology.

Stokes' Shift

Vibrational energy is lost when electrons relax from the excited state back to the ground state. As a result of the energy loss, the emission spectrum of an excited fluorophore is usually shifted to longer wavelengths when compared to the absorption or excitation spectrum. This phenomenon is known as *Stokes' Law* or *Stokes' shift*. Therefore, if Stokes' shift values increase, it becomes easier to separate excitation from emission light through the use of fluorescence filter combinations.

The emission spectral profile (curve) is often a mirror image (or nearly so) of the excitation curve, but shifted to longer wavelengths, as illustrated in Figure 5.3, a useful probe that absorbs light in the yellow-green region and produces yellow-orange emission. In order to achieve maximum fluorescence intensity, a fluorophore is usually excited at wavelengths near or at the peak of the excitation curve, and the widest possible range of emission wavelengths that include the emission peak are selected for detection.

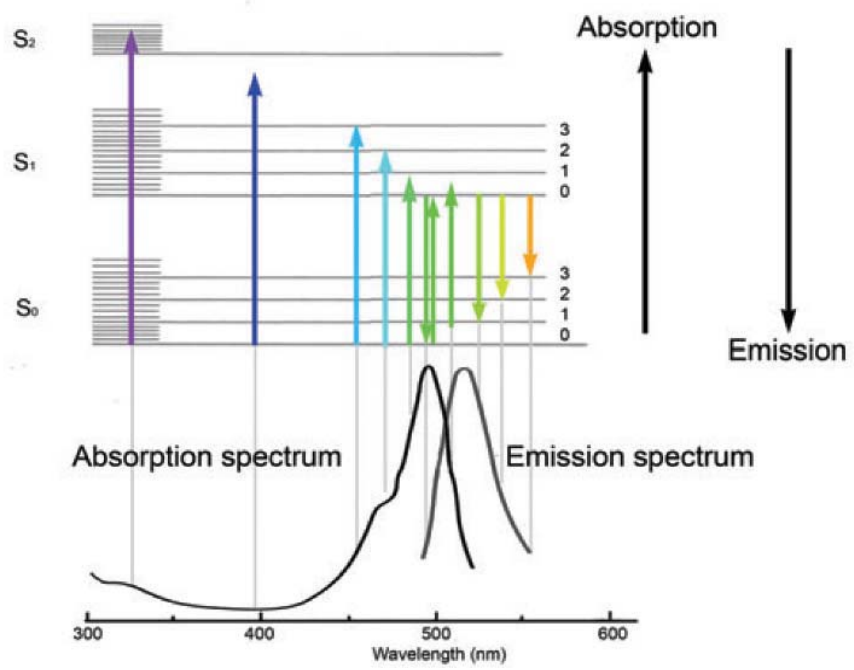

Figure 5.3 Illustration of absorbtion and excitation spectrums of common fluorophores FITC.[130]

The effective separation and detection of excitation and emission wavelengths is achieved in fluorescence microscopy through the proper selection of filters to block or pass specific wavelength bands in the ultraviolet, visible, and near-infrared spectral regions. Fluorescence vertical illuminators are designed with the purpose of controlling the excitation light through the application of readily interchangeable filter (neutral density and interference excitation balancers) insertions into the light path on the way toward the specimen, and again in the path between the specimen and the observation tubes or camera detector system. Perhaps the most important criteria, in view of relatively low fluorescence emission intensities (see discussion above), is that the light source utilized for excitation be of sufficient brightness so that the weak emission light can be maximized, and that the fluorochromes possess adequate absorption properties and emission quantum yields.

The efficiency with which a particular fluorophore absorbs a photon of the excitation light is a function of the molecular cross-section, and the likelihood of absorption is known as the extinction coefficient. Larger extinction coefficients indicate that the absorption of a photon (or quantum) in a given wavelength region is more likely. The quantum yield denotes the ratio of the number of quanta emitted compared to those absorbed (and is usually a value between 0.1 and 1.0). Quantum yield values below 1 are the result of the loss of energy through nonradiative pathways, such as heat or a photochemical reaction, rather than the re-radiative pathway of fluorescence. Extinction coefficient, quantum yield, mean luminous intensity of the light source, and fluorescence lifetime are all important factors that contribute to the intensity and utility of fluorescence emission.

Fluorescence lifetime

The fluorescence lifetime is the characteristic time that a molecule remains in an excited state prior to returning to the ground state and is an indicator of the time available for information to be gathered from the emission profile. During the excited state lifetime, a fluorophore can undergo conformational changes as well as interact with other molecules and diffuse through the local environment. The decay of fluorescence intensity as a function of time in a uniform population of molecules excited with a brief pulse of light is described by an exponential function:

$$I(t) = I_0 \cdot e^{-\frac{t}{\tau}} \tag{5.3}$$

where $I(t)$ is the fluorescence intensity measured at time t,

I(o) is the initial intensity observed immediately after excitation, and

τ is the fluorescence lifetime.

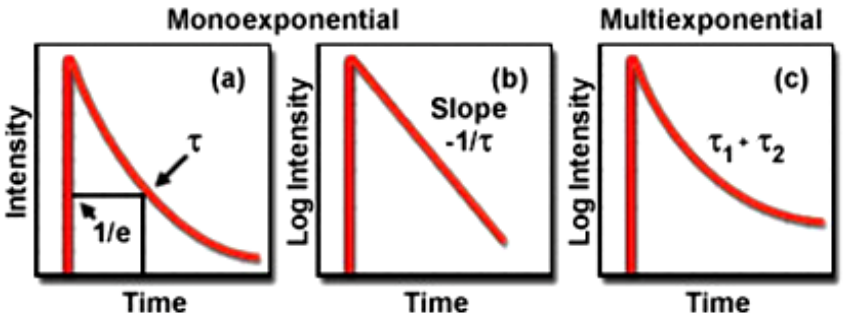

Figure 5.4 Fluorescence lifetime decay profiles.

Formally, the fluorescence lifetime is defined as the time in which the initial fluorescence intensity of a fluorophore decays to *1/e* (approximately 37 percent) of the initial intensity (see Figure 5.4(a)). This quantity is the reciprocal of the rate constant for fluorescence decay from the excited state to the ground state.

Lifetime measurements can be conducted by measuring fluorescence decay after a brief pulse of excitation because the level of fluorescence is directly proportional to the number of molecules in the excited singlet state. In a uniform solvent, fluorescence decay is usually a monoexponential function, as illustrated by the plots of fluorescence intensity as a function of time in Figures 5.4(a) and 5.4(b). More complex systems, such as viable tissues and living cells, contain a mixed set of environments that often yield multiexponential values (Figure 5.4(c)) when fluorescence decay is measured. In addition, several other processes can compete with fluorescence emission for return of

excited state electrons to the ground state, including internal conversion, phosphorescence (intersystem crossing), and quenching. Aside from fluorescence and phosphorescence, non-radiative processes are the primary mechanism responsible for relaxation of excited state electrons.

Many of the common probes employed in optical microscopy have fluorescence lifetimes measured in nanoseconds, but these can vary over a wide range depending on molecular structure, the solvent and environmental conditions. Quantitative fluorescence lifetime measurements enable investigators to distinguish between fluorophores that have similar spectral characteristics but different lifetimes, and can also yield clues to the local environment. Specifically, the pH and concentration of ions in the vicinity of the probe can be determined without knowing the localized fluorophore concentration, which is of significant benefit when used with living cells and tissues where the probe concentration may not be uniform. In addition, lifetime measurements are less sensitive to photobleaching artifacts than are intensity measurements.

Fading, Quenching, and Photobleaching

Many conditions often come into play that ultimately affects the re-radiation of fluorescence emission and thus reduces the intensity. The general term for a reduction of fluorescence emission intensity is *fading*, usually further subdivided into *quenching* and *photobleaching* phenomena for more precise descriptions. Photobleaching is the irreversible decomposition of the fluorescent molecules in the excited state because of their interaction with molecular oxygen before emission. The occurrence of photobleaching is exploited in a technique known as fluorescence recovery after

photobleaching (FRAP), a very useful mechanism for investigating the diffusion and motion of biological macromolecules. The method is based upon photobleaching a sharply defined region of the specimen by an intense burst of laser light, accompanied by the subsequent observation of the rates and pattern of fluorescence recovery in the photobleached area. A related technique, known as fluorescence loss in photobleaching (FLIP), is employed to monitor the decrease of fluorescence in a defined region lying adjacent to a photobleached area. Similar to FRAP, the latter technique is useful in the investigation of molecular mobility and dynamics in living cells.

The excited state relaxation process of quenching results in reduced fluorescence intensity through a variety of mechanisms involving non-radiative energy loss and frequently occurs as a result of oxidizing agents or the presence of salts or heavy metals or halogen compounds. In some cases, quenching results from the transfer of energy to another molecule (termed the acceptor), which resides physically close to the excited fluorophore (the donor), a phenomenon known as fluorescence resonance energy transfer (FRET). This particular mechanism has become the basis for a useful technique involving the study of molecular interactions and associations at distances far below the lateral resolution of the optical microscope.

5.1.2 Fluorescence microscopy

Several investigators reported luminescence phenomena during the seventeenth and eighteenth centuries, but it was British scientist Sir George G. Stokes who first described fluorescence in 1852 and was responsible for coining the term in honor of the blue-white fluorescent mineral fluorite (fluorspar). Fluorescence was first encountered in optical microscopy during the early part of the twentieth century by several notable scientists, including August Kohler and Carl Reichert, who initially reported that fluorescence was a nuisance in ultraviolet microscopy. The first fluorescence microscopes were developed between 1911 and 1913 by German physicists Otto Heimstadt and Heinrich Lehmann as a spin-off from the ultraviolet instrument. These microscopes were employed to observe autofluorescence in bacteria, animal, and plant tissues. In the early 1940s, Albert Coons developed a technique for labeling antibodies with fluorescent dyes, thus giving birth to the field of immunofluorescence. By the turn of the twenty-first century, the field of fluorescence microscopy was responsible for a revolution in cell biology, coupling the power of live cell imaging to highly specific multiple labeling of individual organelles and macromolecular complexes with synthetic and genetically encoded fluorescent probes.

Fluorescence microscopy is an example of the improvements in microscopy that have centered on increasing the contrast between what is interesting (signal) and what is not (background) as it reveals only the objects of interest in dark background.

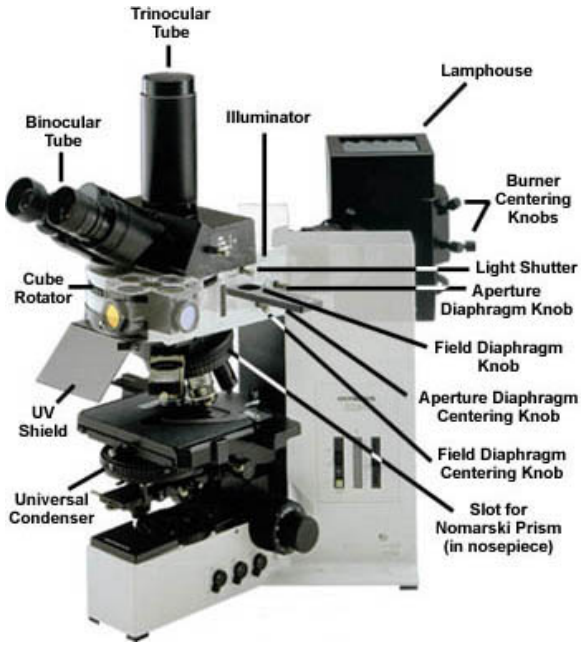

Figure 5.5 Example of conventional fluorescence microscope

Fluorescence microscopy requires that the objects of interest fluoresce. According the Stokes shift, it is easy to imagine how the fluorescence microscope works: illuminates the specimen with one wavelength and filter the return light to only see longer wavelength-shifted fluorescence. The main advantage of the fluorescence microscopy is its compatibility with living cells, which allow dynamic and minimally invasive imaging experiments. However, the main weakness of this microscopy is its spatial resolution, which is limited to ~250 nm. With this spatial resolution, it is impossible to image many small sub-cellular structures. Therefore, many sub diffraction microscopy techniques (such as STED, PALM/STORM and Confocal microscopy) were proposed and studied in recent years. The comparison of the resolutions of recent biological imaging techniques is shown in figure 5.6 [131].

Although the super resolution techniques such as STED and PALM show high resolution, they still have several limitations. For instance, STED requires precise control of the position, phase and amplitude of two laser beams, and its best resolution is restricted to certain dyes able to withstand repeated cycles of excitation and de-excitation at high intensities. The PALM/STORM requires photoswitchable fluorophores and long acquisition times. Proton Induced Fluoescence (PIF) imaging is a break-through technique which is capable of overcoming some of these limitations and, at the same time, maintaining good spatial and temporal resolution.

5.1.3 Purpose of the study

Proton induced fluorescence microscopy is a new technique, and following the use of proton technology in order to fabricate a single cell electroporation biochip, it was deemed interesting to see if we could image the fluorescence in the electroporated cells using the same proton technology. In addition, we also simultaneously investigated the use of proton induced secondary electron (PISE) emission microscopy as a means of cell identification and location. In order to investigate these new forms of microscopy, we first had to fabricate the biochip on an undoped silicon wafer instead of a glass cover slip. This reduced the fluorescence background which would have arisen from the glass cover slip through bombardment with protons. We used a well focused proton beam (~100 nm) for these studies, and the images (both PIF and PISE) are compared with normal fluorescent microscope and SEM images.

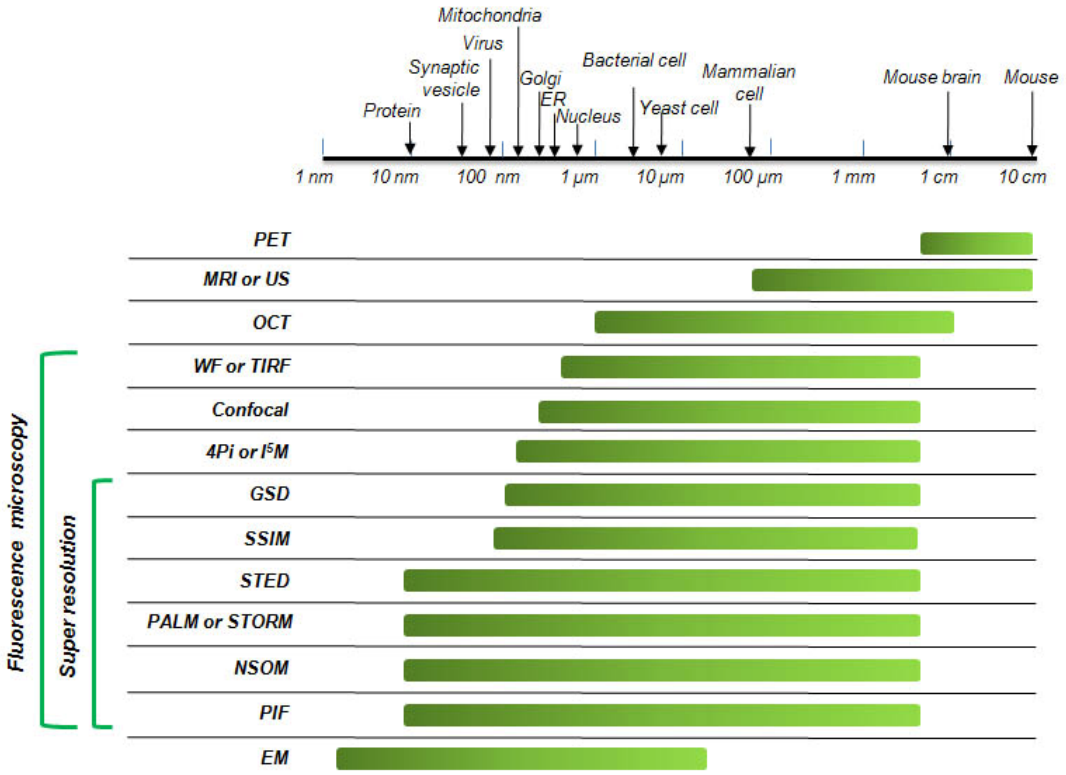

Figure 5.6 Comparison of the spatial and temporal resolutions of biological imaging techniques. Average sizes of biological features are given in logarithmic size scale; specific sizes vary widely among different species and cell lines. The temporal resolution is not applicable (NA) for Electron Microscopy (EM) or Near-Field Scanning Optical Microscopy (NSOM) because they image static samples. Ground-State Depletion (GSD) and Saturated Structured-Illumination Microscopy (SSIM) have not been shown on biological samples, and their temporal resolution are not determined (ND). Endoplasmic Reticulum (ER); Magnetic Resonance Imaging (MRI); Optical Coherence Tomography (OCT); Photoactivated Localization Microscopy (PARM), Stochastic Optical Reconstruction Microscopy (STORM); Positron-Emission Microscopy (PET); Stimulated Emission Depletion (STED); Total Internal Reflection Fluorescence (TIRF); Ultrasound (US); Wide Field Microscopy(WF); Proton Induced Fluorescence (PIF).

5.2 Proton Induced Fluorescence imaging

The nuclear microprobe has a reputation for the utilization of a wide variety of ion beam analytical techniques at spot sizes in the micro/nanometer range. These instruments, although rather complex, have been used to solve a wide range of scientific problems, from microelectronics to biomedicine. One of the techniques which shows considerable promise for the identification of chemical phase, as a check for the presence of certain trace elements, and for monitoring the buildup of ion induced defects in luminescent materials is called Ion Beam Induced Luminescence (IBIL)[132]. This technique has not been applied to biological material or cells, since spatial resolutions until recently have not reached the level which can be achieved using confocal microscopy. Luminescence spectra can be influenced by the relative penetration depth of the various excitation methods. The large penetration depth of MeV ions whilst maintaining spatial resolutions, offers an advantage over keV electrons and for imaging below 250 nm the spatial resolutions of PIF are superior to optical fluorescence. The mechanism of proton induced fluorescence is through interaction with the atomic electrons, which can create atomic and molecular vacancies directly, or indirectly through induced secondary electrons. These vacancies are subsequently filled thereby releasing photons of a fixed wavelength. One advantage of this system over the fluorescence microscope is that background noise is reduced, as the emitted photons from PIF will be only from the fluorescent materials and not scattered from the primary beam.

However, in general, MeV ions cause more damage than photons, and this results in the production of nonradiative recombination centers that offer energetically more favorable de-excitation pathways. This can result in the degradation of the luminescence

yield with ion dose. The relative yields between PIF and conventional fluorescence microscopy, and the differences in bleaching, will not be considered here and will be studied elsewhere.

5.3 Proton induced secondary electron emission

When high energy protons hit the surface of a material, their interaction generates secondary electrons. Even though the secondary electrons induced in proton/electron collisions have low energy, by using a channel electron multiplier (CEM) detector with its ability to detect single electrons, we are able to image surface structures on the material with high contrast, sensitivity and resolution. This gives a similar image to scanning electron microscopy (SEM), although at not such high resolutions. However, this imaging technique is useful for locating the cell, with the added advantage that PIF images can be generated simultaneously.

5.4 Equipment and methods

Biochip fabrication

The substrate material for biochip was changed from glass cover slip to undoped silicon wafer to remove high fluorescence background from the glass. Tests have shown that, unlike the glass cover slip, the undoped silicon wafer does not give any fluorescent signal when it is scanned by proton beam, and this characteristic makes the undoped wafer most suitable candidate for the fluorescence imaging purpose. The piece of silicon wafer was cut to a small square shape, 2×2 cm^2. The fabrication procedures are similar to those described previously for the biochips fabricated on the cover slip. Figure 5.7 shows the biochips fabricated on the silicon wafer.

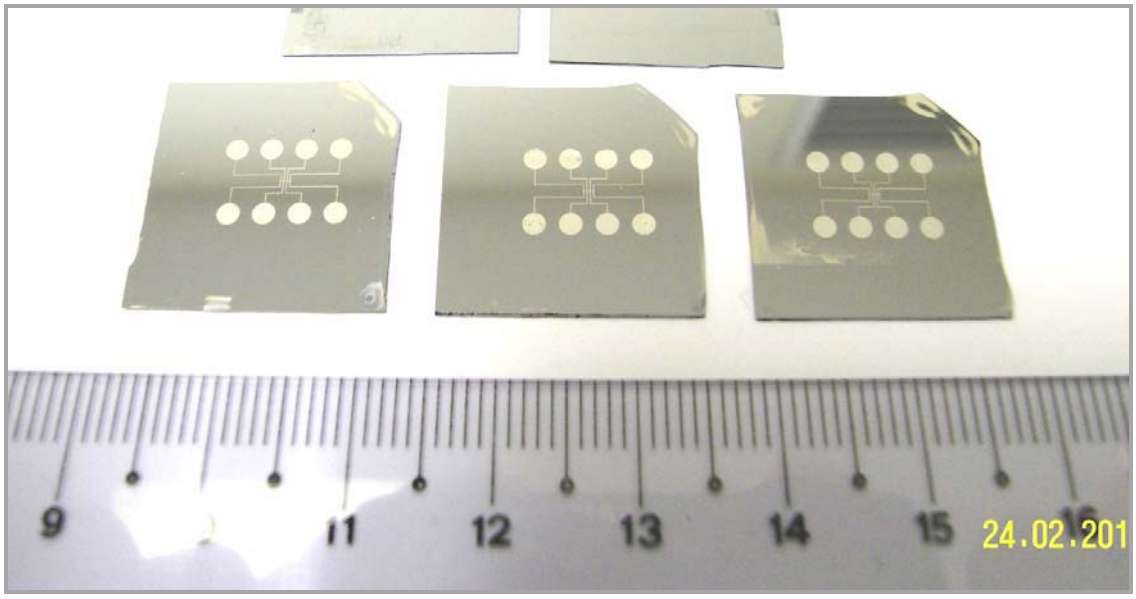

Figure 5.7 The electroporation biochip made on the undoped silicon wafer.

Electroporation

The electroporation was performed using the same conditions as reported in chapter 4, but using the optimized parameters. However, only the SYTOX® Green step was used in order to introduce the fluorescent molecules to penetrate the cells. After the electroporation, the critical point drying process was then used to dry the sample before imaging. For the critical point drying the water in the cells is replaced with ethanol, and so the cells were then replaced with a series of ethanol, 25% for 3 min, 50% for 3 min, 75% for 3 min, 95% for 3 min, 100% for 5 min. The biochips were then transferred to a Critical Point Dryer (BAL-TEC CPD 030) for 1 hr (samples were placed in small porous containers to ensure that they were not damaged by excessive pressure variations during the drying process).

The preliminary high resolution PIF work was carried out using the PBW beam line (the 10 degree beam line), where the target chamber was modified slightly to incorporate a photomultiplier (PM) tube. The biochip was mounted on the target holder on which was placed a Hamamatsu PM tube R7402 with lens (see appendix A) to measure the PIF signals. A CEM detector was placed in front of the target in order to measure the secondary electrons. A schematic diagram of this set up is shown in figure 5.8.

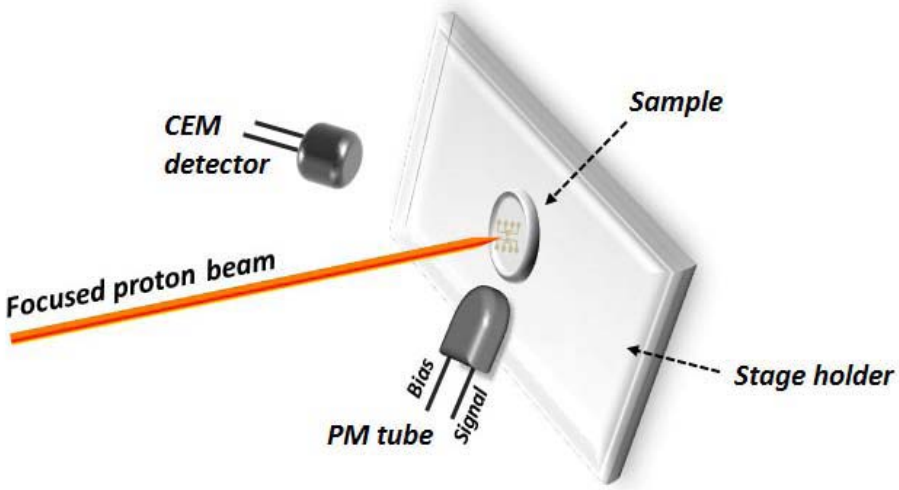

Figure 5.8 Illustration of the PIF and PISE system at 10 degree chamber. The photomultiplier tube (Hamamatsu R7402) is mounted on the sample holder in front of the sample, while the CEM is mounted in the chamber.

Imaging

The imaging was performed after the beam focusing down to ~100 nm. The in-house program called *IonDAQ*, developed by Dr.Chammika Udalagama, was used to collect the data. The beam is scanned raster style over a predetermined region and the PIF and PISE data recorded for each pixel in the scan. Images of both PIF and PISE can then be assembled using software. We have scanned using 256×256 pixels with a 5000-6000 μs update time for each pixel, and hence the total scan time is around 20-25 min for each 20 μm scan-size image.

5.5 Results and discussion

Preliminary experiments on imaging with a focused proton beam were carried out. We were able to observe the electrodes from the large scan size image (see figure 5.9) in which there are clearly observed cells outside and also in between the electrodes. Figure 5.9 (a)~(e) show the imaging results from different techniques; bright and dark field optical microscopy, PIF, PISE and SEM images. Figure (c) and (d) show images of 300 μm size. The fluorescent cells on the biochip surface were clearly seen with the optical microscope (figure (b)) and by PIF (figure (c)). An interesting observation is that the edges of the electrodes are highlighted in the PIF image, but not with the fluorescence microscope. The reason for this is not obvious; although luckily it help the visualization: The problem expected when carrying out PIF is locating the correct cells since the substrate is not transparent.

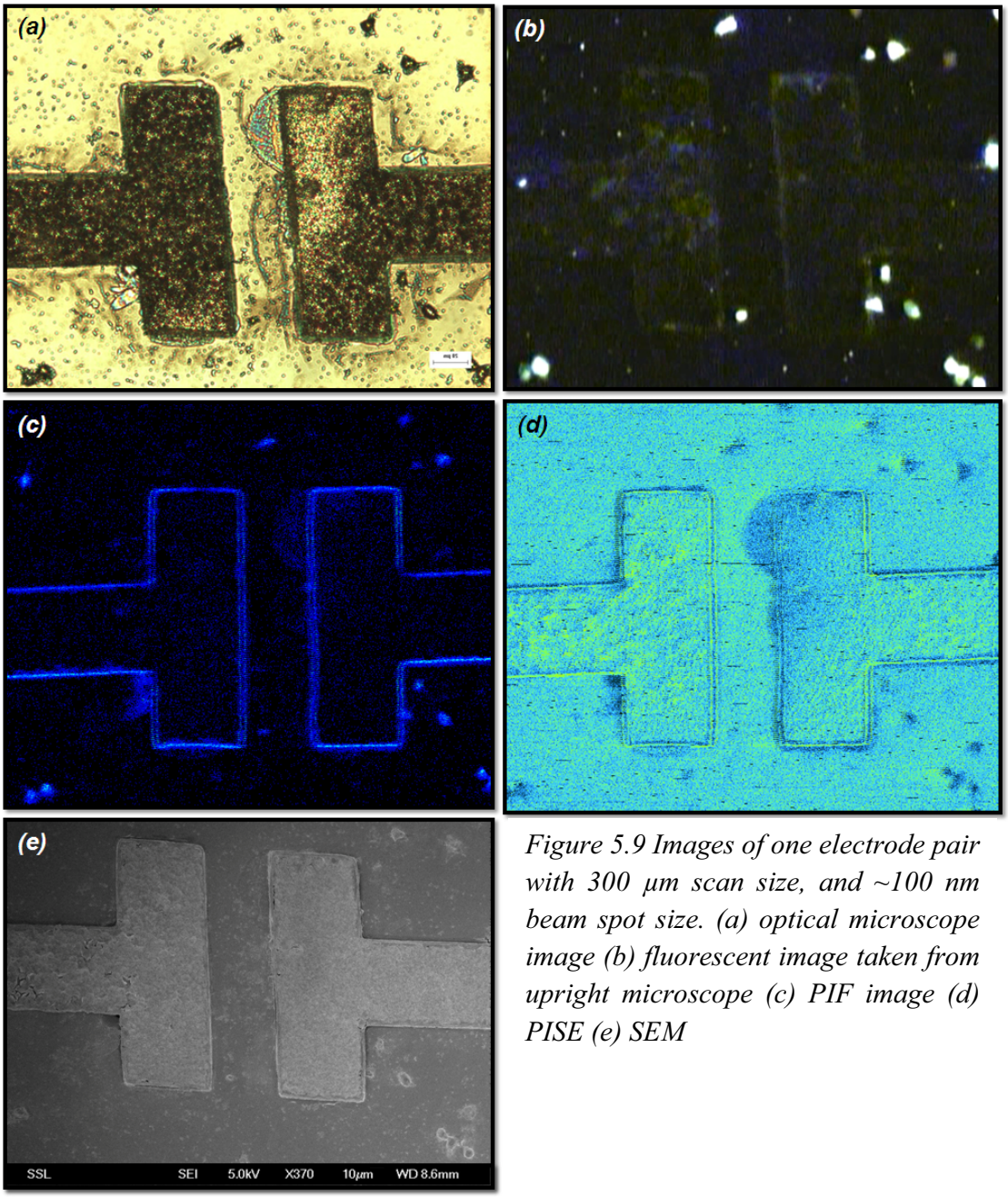

Figure 5.9 Images of one electrode pair with 300 μm scan size, and ~100 nm beam spot size. (a) optical microscope image (b) fluorescent image taken from upright microscope (c) PIF image (d) PISE (e) SEM

One single fluorescent electroporated cell can be seen clearly at the bottom region between the gap (see figure 5.9). This cell was then imaged with a smaller scan size of 30 μm with 5000 μs update time (see figure 5.10). The PIF and PISE images show reasonable details and contrast when comparing with microscope, fluorescent microscope and SEM images. We also carried out similar imaging with another cell in between another electrode gap (see figure 5.11), and a random cell outside the gaps (see figure 5.12). Figure 5.11 shows the cell which is very close to one electrode; where surprisingly the electrode can be seen very clearly with PIF. The images from figure 5.11 and 5.12 show similar results, particularly figure 5.12 where PIF gives better resolution than the fluorescence microscope.

The SEM image, as expected, has better resolution than PISE, although the sample for SEM required a conducting layer of gold to avoid charging. This is not necessary for PISE since surface charging does not appear to be a problem.

Comparing between electroporated and non-electroporated cells, the nucleus of electroporated cells are seen more obvious and the cells are slightly smaller. This may be due to the fact that the cells are slightly raised from the surface after electroporation due to a reduction in adherence.

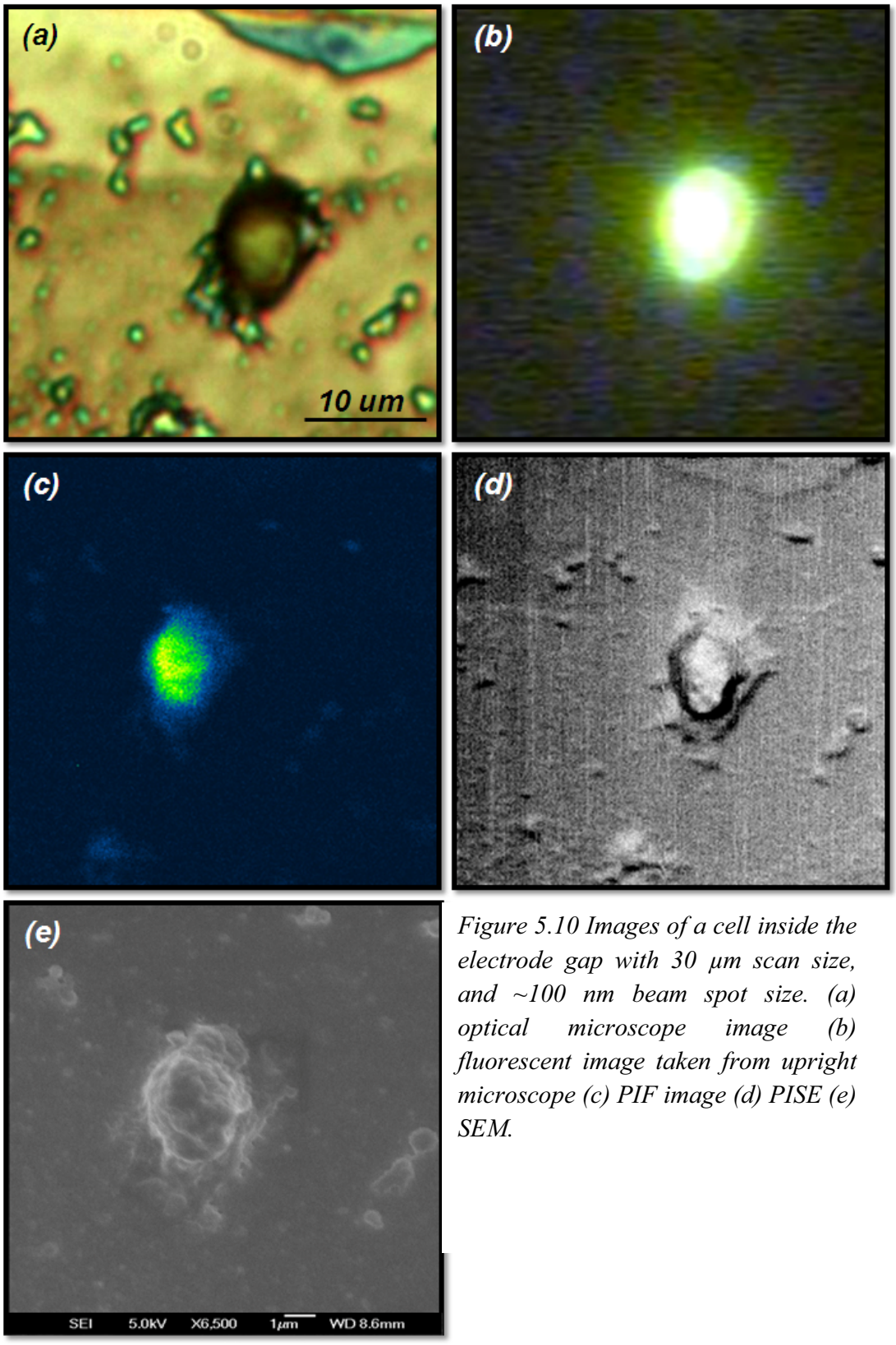

Figure 5.10 Images of a cell inside the electrode gap with 30 μm scan size, and ~100 nm beam spot size. (a) optical microscope image (b) fluorescent image taken from upright microscope (c) PIF image (d) PISE (e) SEM.

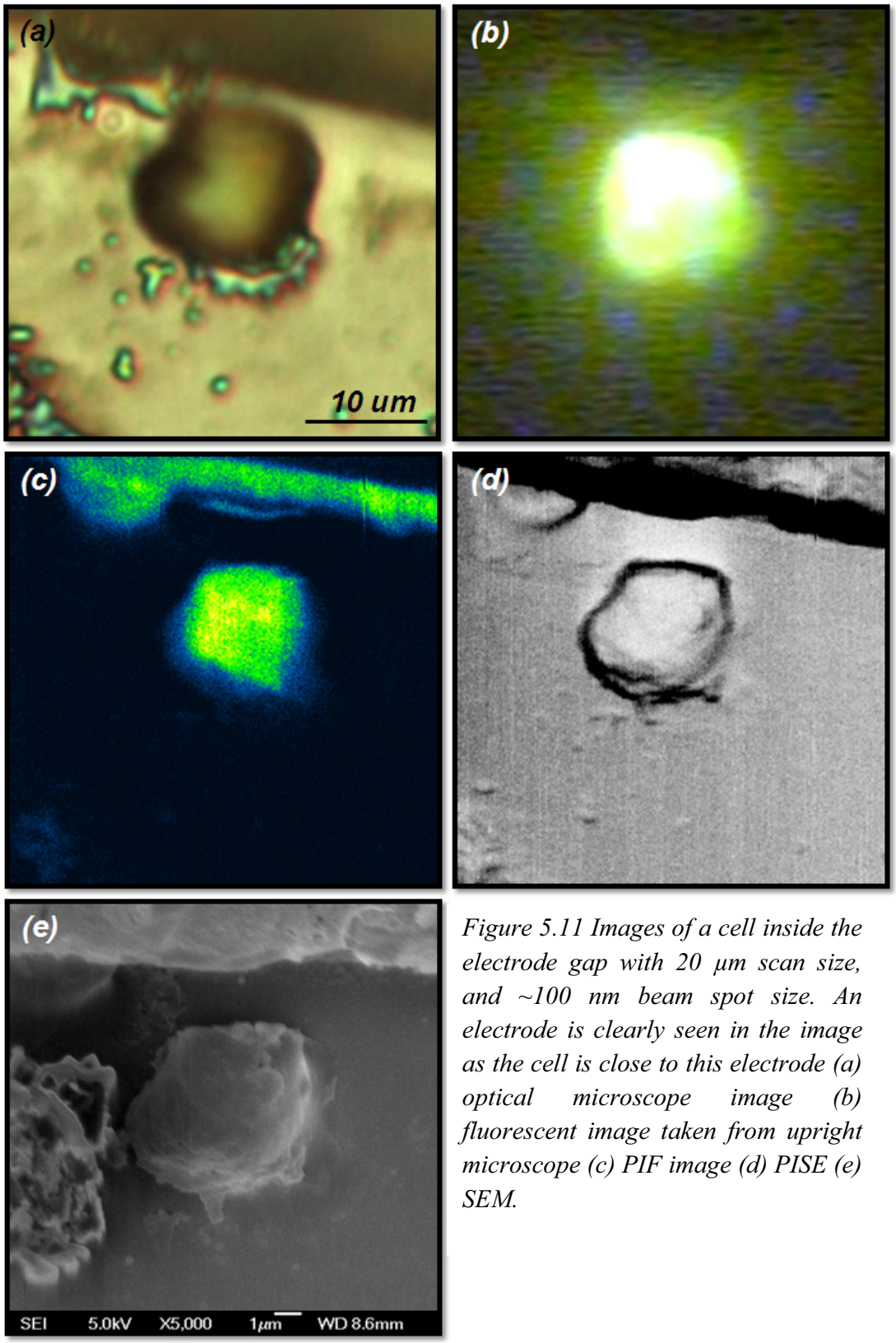

Figure 5.11 Images of a cell inside the electrode gap with 20 μm scan size, and ~100 nm beam spot size. An electrode is clearly seen in the image as the cell is close to this electrode (a) optical microscope image (b) fluorescent image taken from upright microscope (c) PIF image (d) PISE (e) SEM.

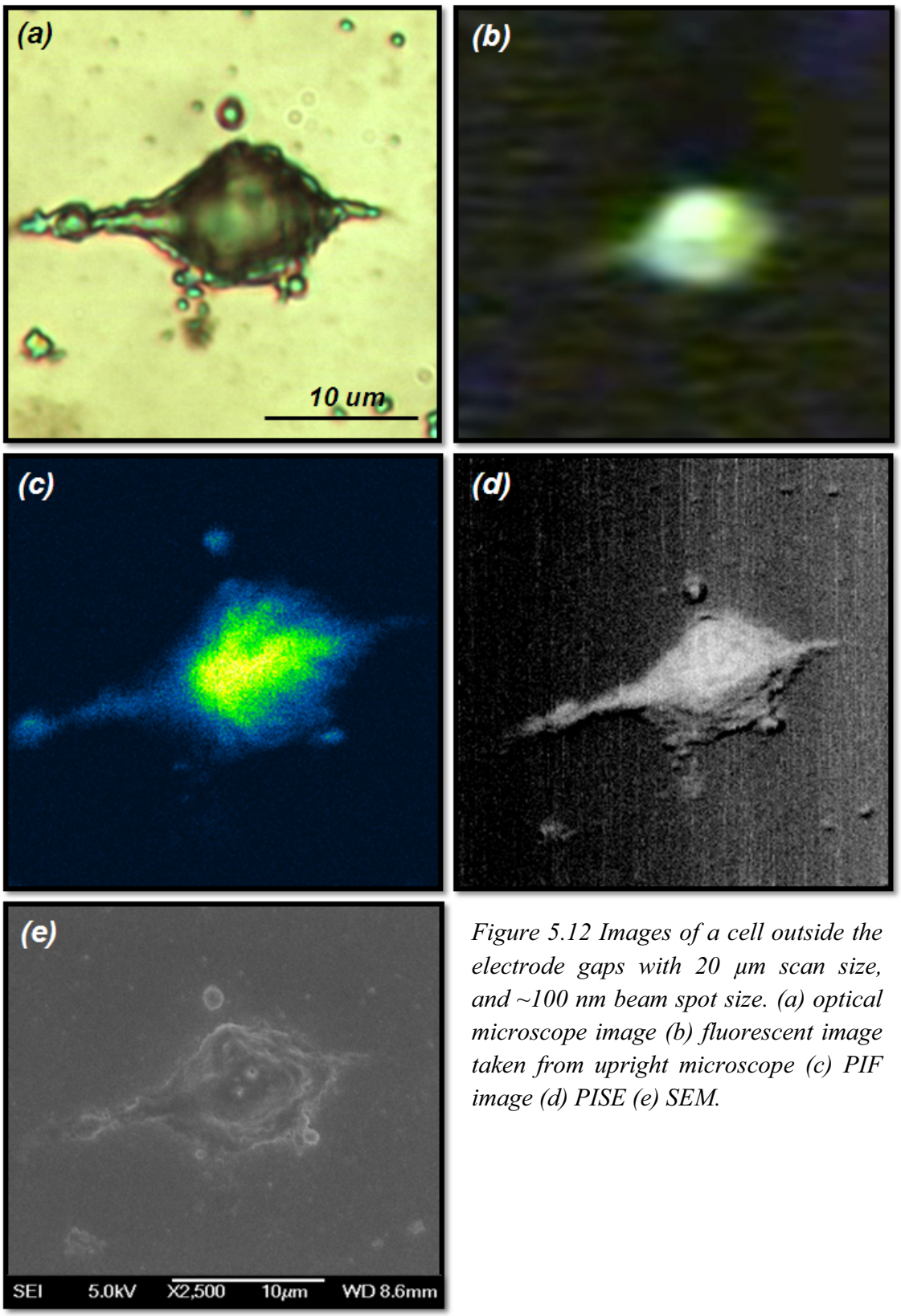

Figure 5.12 Images of a cell outside the electrode gaps with 20 μm scan size, and ~100 nm beam spot size. (a) optical microscope image (b) fluorescent image taken from upright microscope (c) PIF image (d) PISE (e) SEM.

5.6 Conclusion

PIF images of electroporated cells were successfully taken using the modified PBW facility in CIBA. With a well focused proton beam, relatively high resolution images were achieved (~100 nm). In our experiment, PIF gives slightly better resolution than standard fluorescent microscopy due to the beam spot size of 100 nm being less than the diffraction limits of the standard optically based technique. PISE also shows one advantage over the SEM technique, that of not requiring a conductive layer to avoid charging, although the spatial resolutions of SEM are, as expected, superior. Nevertheless, PISE can be used effectively for cell location, identification, and positioning.

From these preliminary results, PIF has been shown to be an interesting technique with high potential, since the spatial resolutions achievable in whole cells are dependent only on the beam spot size. A new beam line at CIBA dedicated to single cell imaging is expected to give much better resolution and is especially designed for imaging cells.

Chapter 6

Overall Conclusion

Electroporation has been studied for over two decades and has many applications in cellular biology and biotechnology for gene transfer and loading of cells with extracellular molecules, also in medicine for gene therapy, cancer chemotherapy and transdermal drug delivery.

A novel electroporation micro biochip was fabricated and reported in this thesis. For the fabrication of this electroporation biochip, consisting of 4 pairs of 7 um-thick nickel microelectrodes on the glass cover slip surface which was used as a substrate because of its nonconductive property. The conductive structure consisted of eight conductive circular pads, 1800 um diameter-size. These circular pads connect to electrodes located in the middle of the biochips using conducting lines, and the gap between each pair of electrodes was designed to perform the electroporation. The gaps were 50 um in size were much smaller than conventional electroporators. These small gaps, across which electrical pulses were applied, resulted in larger and more uniform electric field distributions. The Proton Beam Writing (PBW) technique was used in the fabrication process, since PBW is capable of fabricating well defined high aspect ratio structures with straight and smooth side wall and is ideal for 3D electrode production. Moreover,

unlike other reported electroporation biochips, our biochip can be reused (tests have shown approximately 24 times). The electroporation biochips were tested using N2a cells, which can be successfully seeded onto the chips in healthy condition.

In this thesis we also aimed to demonstrate the effectiveness of our biochip for single-cell electroporation. The chip could enhance *in vitro* particle introduction to specific cells. The experiments were conducted using two fluorescent stains, Sytox® Green and Ethidium homodimer 2, on N2a cells with three varied parameters; pulse amplitudes, number of pulses, and pulse width. The Ethidium homodimer 2 was used to indicate the resealing of the cell. The optimised transmembrane voltage across the electroporated membrane was achieved at ~0.85 V. This result agrees with the voltage range (0.2-1.5V) of dielectric breakdown suggested by the published data [76]. With our efficient and easy-to-use biochip and optimized parameters, excellent transfection and survival rates were achieved at 82.1% and 86.7%, respectively. These rates were higher in both transfection efficiency and cell viability than conventional electroporators and most reported microelectroporators. This result provided data for the efficient introduction of impermeant materials, such as drugs, DNA and protein, into individual cells.

Since our single-cell electroporation biochip showed that it successfully electroporated cells and introduced outside particles into cells, it is deemed to be a promising tool for gene delivery and useful for investigating the mechanism of gene transfection. With our single-cell electroporation biochips, future investigations could target fundamental kinetic and thermodynamic properties of electric-field-induced pore formation and properties of transpore mass transport, and diffusion. Compared to the

commercial electroporation equipment, for these types of studies our electroporation biochip is more advantages in the following aspects:

(a) Less required cells and plasmids,

(b) Lower electroporation voltages,

(c) Simpler cell culturing, and

(d) Concentrating particles to specific cells.

The thesis describes the first studies which demonstrate single-cell electroporation in N2a cells. Since these neuroblastoma cells were used as a model system to study neuronal differentiation [128], our study could pave the way for the recognition of the regulation of neural cell development.

Although single-cell electroporation has high potential for research into cell membrane transport, this type of research is still at an early stage. Due to time constraints, only 3 most important parameters had been considered in this study. There are other minor parameters such as an oxidization of electrode, temperature, buffer composition and wave form which can be considered and optimized in the future so as to achieve even higher transfection rate. Future studies may also include different cell lines and a wider variety of electroporated materials.

The effects of cell deformation on electroporation can also be addressed. Membrane tension contributes to the critical energy density necessary for dielectric breakdown [133]. Akinlaja and Sachs showed that, while short pulses (50 μs) breakdown was dependent on tension, at longer pulses (50–100 ms) the voltage required for breakdown was tension independent. They suggest that the mechanism for low field/long pulses is

different from that of high field/short pulses [134]. Our pulses are in the millisecond range and therefore we assumed that the breakdown is not greatly affected by tension. Nevertheless, further investigation must be pursued to resolve the mechanism responsible for breakdown at longer pulses.

The PIF and PISE techniques were utilized for the first time to image electroporated cells and normal cell stained with SYTOX® Green on the fabricated silicon biochip. With a well focused proton beam (~100 nm), the system gave good resolution and contrast images from both techniques. The PIF shows better resolution compared with standard fluorescence microscopy, since fluorescence microscopy has limits caused by the diffraction of light.

Using high energy protons, the PISE shows high contrast and the surface features of the cells can be clearly observed. Although the resolution of SEM is undoubtedly higher, PISE can be utilised effectively for identification and location of the cells. In addition PISE can be improved since this experiment was of a highly investigative nature, and many PISE experimental parameters could be further optimised, i.e. beam spot size, to improve the resolution.

Our preliminary results demonstrated that PIF has a capability to image small biological samples with better quality than many commercial techniques. Further studies and development will undoubtedly make PIF a leading fluorescence imaging technique in the future and may pave the way to interesting findings in the biological and medical fields in the near future.

Bibliography

[1] K. E. Petersen, "Silicon as a mechanical material : Kurt E. Petersen. Proc. IEEE70 (5), 420 (1982)," *Microelectronics Reliability,* vol. 23, pp. 403-403, 1983.

[2] K. D. Wise and K. Najafi, "MICROFABRICATION TECHNIQUES FOR INTEGRATED SENSORS AND MICROSYSTEMS," *Science,* vol. 254, pp. 1335-1342, Nov 1991.

[3] M. Ferrari, "BioMEMS and Biomedical Nanotechnology," *Springer,* vol. VI: Biomedical & Biological Nanotechnology. V2: Micro/Nano Technology for Genomics and Proteomics. V3: Therapeutic Micro/Nanotechnology. V4: Biomolecular Sensing, Processing and Analysis, 2007.

[4] R. Bashir, "BioMEMS: state-of-the-art in detection, opportunities and prospects," *Advanced Drug Delivery Reviews,* vol. 56, pp. 1565-1586, 2004.

[5] F. Watt, "Focused high energy proton beam micromachining: A perspective view," *Nuclear Instruments and Methods in Physics Research Section B: Beam Interactions with Materials and Atoms,* vol. 158, pp. 165-172, 1999.

[6] P. Rai-Choudhury*, et al.*, "Handbook of Microlithography, Micromachining, and Microfabrication, Vol. 1, Ch. 3," *SPIE Press Monograph PM 39,* p. 11, 1997.

[7] J. S. Wilczynski, "Optical step and repeat camera with dark field automatic alignment," *Journal of Vacuum Science and Technology,* vol. 16, pp. 1929-1933, 1979.

[8] W. Waldo, "Techniques and Tools for Optical Lithography," in *Handbook of VLSI Microlithography (Second Edition)*, N. H. John, Ed., ed Norwich, NY: William Andrew Publishing, 2001, pp. 472-643.

[9] J. G. Goodberlet and B. L. Dunn, "Deep-ultraviolet contact photolithography," *Microelectronic Engineering,* vol. 53, pp. 95-99, 2000.

[10] J. G. N. LaBianca, K. Lee, E. Sullivan and J. Shaw, "High Aspect Ratio Optical Resist Chemistry for MEMS Applications," *4th Int. Symp. on Magnetic Materials, Processes, and Devices, The Electrochem. Soc.,* vol. 95-18 pp. 386–396, 1995.

[11] S. Hector and P. Mangat, "Review of progress in extreme ultraviolet lithography masks," Washington, DC (USA), 2001, pp. 2612-2616.

[12] D. L. Spears and H. I. Smith, "High-resolution pattern replication using soft X-rays," *Electron. Lett. ,* vol. 8, 1972.

[13] E. P. Cotte*, et al.*, "Predicting mechanical distortions in x-ray masks," Santa Clara, CA, USA, 1999, pp. 429-440.

[14] M. F. Laudon*, et al.*, "MECHANICAL RESPONSE OF X-RAY MASKS," *Japanese Journal of Applied Physics Part 1-Regular Papers Short Notes & Review Papers,* vol. 32, pp. 5928-5932, Dec 1993.

[15] M. P. Schlax*, et al.*, "Dynamic characterization of step-induced vibrations of x-ray mask membranes," Santa Clara, CA, USA, 1998, pp. 629-637.

[16] R. L. Seliger*, et al.*, "A high-intensity scanning ion probe with submicrometer spot size," *Applied Physics Letters,* vol. 34, pp. 310-312, 1979.

[17] B. A. Free and G. A. Meadows, "Projection in lithography with aperture lenses," *J. Vac. Sci. Technol.,* vol. 15, p. 1028, 1978.

[18] G. Stengl*, et al.*, "Ion projection system for IC production," *J. Vac. Sci. Technol. ,* vol. 16, p. 1883, 1979.

[19] J. Melngailis, "Ion Beam Lithography," in *Encyclopedia of Materials: Science and Technology*, K. H. J. Buschow*, et al.*, Eds., ed Oxford: Elsevier, 2001, pp. 4274-4280.

[20] I. Brodie and J. J. Muray, "The physics of micro-nano-fabrication," *SRI International, Menlo Park, California, Plenum Press, New York,* p. 491, 1992.
[21] F. Watt*, et al.*, "ION BEAM LITHOGRAPHY AND NANOFABRICATION: A REVIEW " *International Journal of Nanoscience* vol. 4, pp. 269-286, 2005.
[22] G. Owen, "Electron lithography for the fabrication of microelectronic devices," *Rep. Prog. Phys.,* vol. 48, pp. 795-851, 1985.
[23] A. N. Broers and T. H. P. Chang, "High Resolution Lithography for Microcircuits," *Research Report RC-7403 (31860), IBM T. J. Watson Research Center, Yorktown Heights, NY,* 1978.
[24] P. R. Thornton, "Electron physics in device microfabrication, I: General background and scanning systems," *Adv. Electron. Electron Phys.,* vol. 48, 1979.
[25] F. Watt*, et al.*, "Proton beam writing," *Materials Today,* vol. 10, pp. 20-29, 2007.
[26] "www.feicompany.com."
[27] J. Meingaills, "Critical review: focused ion beam technology and applications," *J. Vac. Sci. Technol. B,* vol. 5, pp. 469-495, 1987.
[28] K. Edinger, "Focused Ion Beams for Direct Writing," in *Direct-Write Technologies for Rapid Prototyping*, ed San Diego: Academic Press, 2002, pp. 347-383.
[29] J. A. van Kan*, et al.*, "Proton beam micromachining: a new tool for precision three-dimensional microstructures," *Sensors and Actuators A: Physical,* vol. 92, pp. 370-374, 2001.
[30] J. A. van Kan*, et al.*, "Three-dimensional nanolithography using proton beam writing," *Applied Physics Letters,* vol. 83, pp. 1629-1631, 2003.
[31] J. A. van Kan*, et al.*, "Sub 100 nm proton beam micromachining: theoretical calculations on resolution limits," *Nuclear Instruments and Methods in Physics Research Section B: Beam Interactions with Materials and Atoms,* vol. 161-163, pp. 366-370, 2000.
[32] C. N. B. Udalagama*, et al.*, "A Monte Carlo study of the extent of proximity effects in e-beam and p-beam writing of PMMA," *Nuclear Instruments and Methods in Physics Research Section B: Beam Interactions with Materials and Atoms,* vol. 260, pp. 384-389, 2007.
[33] W. Hu*, et al.*, "Sub-10 nm electron beam lithography using cold development of poly(methylmethacrylate)," *Journal of Vacuum Science & Technology B: Microelectronics and Nanometer Structures,* vol. 22, pp. 1711-1716, 2004.
[34] J. A. van Kan*, et al.*, "Proton Beam Writing of Three-Dimensional Nanostructures in Hydrogen Silsesquioxane," *Nano Letters 2006* vol. 6, pp. 579-582 2006.
[35] T. Tryfona and M. T. Bustard, "Enhancement of biomolecule transport by electroporation: A review of theory and practical application to transformation of <I>Corynebacterium glutamicum</I>," *Biotechnology and Bioengineering,* vol. 93, pp. 413-423, 2006.
[36] J. de Gier, "Permeability barriers formed by membrane lipids," *Bioelectrochemistry and Bioenergetics,* vol. 27, pp. 1-10, 1992.
[37] D. García*, et al.*, "Pulsed electric fields cause bacterial envelopes permeabilization depending on the treatment intensity, the treatment medium pH and the microorganism investigated," *International Journal of Food Microbiology,* vol. 113, pp. 219-227, 2007.
[38] M. M. Ponpipom*, et al.*, "Cell-specific ligands for selective drug delivery to tissues and organs," *Journal of Medicinal Chemistry,* vol. 24, pp. 1388-1395, 1981.
[39] A. L. Boyd and D. Samid, "Review: molecular biology of transgenic animals," *J Anim Sci,* vol. 71 Suppl 3, pp. 1-9, 1993.
[40] D. J. Wells, "Gene Therapy Progress and Prospects: Electroporation and other physical methods," *Gene Ther,* vol. 11, pp. 1363-1369, 2004.
[41] S. A. Abdulhaqq and D. B. Weiner, "DNA vaccines: developing new strategies to enhance immune responses," *Immunol Res,* vol. 42, pp. 219-32, 2008.

[42] I. Hapala, "Breaking the Barrier: Methods for Reversible Permeabilization of Cellular Membranes," *Critical Reviews in Biotechnology,* vol. 17, pp. 105-122, 2008.

[43] R. Arav and I. Friedberg, "Combined effects of ATP and its analogs on the membrane permeability in transformed mouse fibroblasts," *FEBS Letters,* vol. 387, pp. 149-151, 1996.

[44] G. Ahnert-Hilger*, et al.*, "Poration by alpha-toxin and streptolysin O: an approach to analyze intracellular processes," *Methods Cell Biol,* vol. 31, pp. 63-90, 1989.

[45] P. Seibel*, et al.*, "Transfection of mitochondria: strategy towards a gene therapy of mitochondrial DNA diseases," *Nucleic Acids Res,* vol. 23, pp. 10-7, Jan 11 1995.

[46] J. Gruenberg and F. R. Maxfield, "Membrane transport in the endocytic pathway," *Curr Opin Cell Biol,* vol. 7, pp. 552-63, Aug 1995.

[47] R. M. Sandri-Goldin*, et al.*, "High-efficiency transfer of DNA into eukaryotic cells by protoplast fusion," *Methods Enzymol,* vol. 101, pp. 402-11, 1983.

[48] D. J. Jolly*, et al.*, "High-efficiency gene transfer into cells," *Methods Enzymol,* vol. 149, pp. 10-25, 1987.

[49] K. W. Culver and R. M. Blaese, "Gene therapy for cancer," *Trends Genet,* vol. 10, pp. 174-8, May 1994.

[50] P. L. McNeil, "Incorporation of macromolecules into living cells," *Methods Cell Biol,* vol. 29, pp. 153-73, 1989.

[51] P. L. McNeil and E. Warder, "Glass beads load macromolecules into living cells," *J Cell Sci,* vol. 88 (Pt 5), pp. 669-78, Dec 1987.

[52] Y. Noda*, et al.*, "A new method for permeabilization of the plasma membrane of cultured mammalian cells. VII. Permeabilization of growing and resting cells by vortex-stirring with high molecular weight polyacrylic acid," *Biol Pharm Bull,* vol. 19, pp. 1565-9, Dec 1996.

[53] N. Shimizu and Y. Kawazoe, "A new method for permeabilization of cultured cells without cell damage," *Biol Pharm Bull,* vol. 19, pp. 484-6, Mar 1996.

[54] M. S. Clarke and P. L. McNeil, "Syringe loading introduces macromolecules into living mammalian cell cytosol," *J Cell Sci,* vol. 102 (Pt 3), pp. 533-41, Jul 1992.

[55] A. S. Waldman and B. C. Waldman, "Stable transfection of mammalian cells by syringe-mediated mechanical loading of DNA," *Anal Biochem,* vol. 258, pp. 216-22, May 1 1998.

[56] H. Soreq and S. Seidman, "Xenopus oocyte microinjection: from gene to protein," *Methods Enzymol,* vol. 207, pp. 225-65, 1992.

[57] M. S. Clarke*, et al.*, "Cytoplasmic loading of dyes, protein and plasmid DNA using an impact-mediated procedure," *Biotechniques,* vol. 17, pp. 1118-25, Dec 1994.

[58] J. C. Sanford*, et al.*, "DELIVERY OF SUBSTANCES INTO CELLS AND TISSUES USING A PARTICLE BOMBARDMENT PROCESS," *Particulate Science and Technology: An International Journal,* vol. 5, pp. 27 - 37, 1987.

[59] R. M. Klein*, et al.*, "High-velocity microprojectiles for delivering nucleic acids into living cells. 1987," *Biotechnology,* vol. 24, pp. 384-6, 1992.

[60] J. C. Sanford*, et al.*, "Optimizing the biolistic process for different biological applications," *Methods Enzymol,* vol. 217, pp. 483-509, 1993.

[61] E. Preininger*, et al.*, "A new approach for the biolistic method: Bombardment of living nitrogen-fixing bacteria into plant tissues," *In Vitro Cellular & Developmental Biology-Plant,* vol. 39, pp. 443-449, Sep-Oct 2003.

[62] E. Neumann*, et al.*, "GENE-TRANSFER INTO MOUSE LYOMA CELLS BY ELECTROPORATION IN HIGH ELECTRIC-FIELDS," *Embo Journal,* vol. 1, pp. 841-845, 1982.

[63] S. Orlowski and L. M. Mir, "Cell electropermeabilization: a new tool for biochemical and pharmacological studies," *Biochimica et Biophysica Acta (BBA) - Reviews on Biomembranes,* vol. 1154, pp. 51-63, 1993.

[64] R. Heller, "The development of electroporation," *Science,* vol. 295, pp. 277-277, Jan 2002.
[65] C. M. Wu*, et al.*, "Regulated, electroporation-mediated delivery of pro-opiomelanocortin gene suppresses chronic constriction injury-induced neuropathic pain in rats," *Gene Therapy,* vol. 11, pp. 933-940, Jun 2004.
[66] A. Peister*, et al.*, "Stable transfection of MSCs by electroporation," *Gene Therapy,* vol. 11, pp. 224-228, Jan 2004.
[67] H. L. Withers, "Direct Plasmid Transfer Between Bacterial Species and Electrocuring." vol. 47, ed, 1995, pp. 47-54.
[68] L. Gunn*, et al.*, "Transfer of Episomal and Integrated Plasmids from Saccharomyces cerevisiae to Escherichia coli by Electroporation." vol. 47, ed, 1995, pp. 55-66.
[69] H. Weber and H. Berg, "Electrofusion of Yeast Protoplasts." vol. 47, ed, 1995, pp. 93-104.
[70] M. R. Prausnitz*, et al.*, "Electroporation of mammalian skin: a mechanism to enhance transdermal drug delivery," *Proceedings of the National Academy of Sciences of the United States of America,* vol. 90, pp. 10504-10508, November 15, 1993 1993.
[71] L. L. Tang*, et al.*, "Apoptosis induction with electric pulses - A new approach to cancer therapy with drug free," *Biochemical and Biophysical Research Communications,* vol. 390, pp. 1098-1101, Dec 2009.
[72] L. Grossin*, et al.*, "Gene therapy in cartilage using electroporation," *Joint Bone Spine,* vol. 70, pp. 480-482, 2003.
[73] U. Zimmermann*, et al.*, "Dielectric breakdown of cell membranes," *Biophys J,* vol. 14, pp. 881-99, Nov 1974.
[74] E. Neumann and K. Rosenheck, "Permeability changes induced by electric impulses in vesicular membranes," *Journal of Membrane Biology,* vol. 10, pp. 279-290, 1972.
[75] J. C. Weaver and Y. A. Chizmadzhev, "Theory of electroporation: A review," *Bioelectrochemistry and Bioenergetics,* vol. 41, pp. 135-160, Dec 1996.
[76] J. C. Weaver, "ELECTROPORATION - A GENERAL PHENOMENON FOR MANIPULATING CELLS AND TISSUES," *Journal of Cellular Biochemistry,* vol. 51, pp. 426-435, Apr 1993.
[77] S.-C. Yang*, et al.*, "Determination of optimum gene transfection conditions using the Taguchi method for an electroporation microchip," *Sensors and Actuators B: Chemical,* vol. 132, pp. 551-557, 2008.
[78] P. F. Baker and D. E. Knight, "Calcium-dependent exocytosis in bovine adrenal medullary cells with leaky plasma membranes," *Nature,* vol. 276, pp. 620-622, 1978.
[79] K. Kinosita and T. T. Tsong, "Hemolysis of human erythrocytes by transient electric field," *Proceedings of the National Academy of Sciences of the United States of America,* vol. 74, pp. 1923-1927, May 1977 1977.
[80] B. Gauger and F. W. Bentrup, "A study of dielectric membrane breakdown in theFucus egg," *Journal of Membrane Biology,* vol. 48, pp. 249-264, 1979.
[81] R. Benz*, et al.*, "Reversible electrical breakdown of lipid bilayer membranes: a charge-pulse relaxation study," *J Membr Biol,* vol. 48, pp. 181-204, Jul 16 1979.
[82] S. Jayaram*, et al.*, "Effects of high electric field pulses on Lactobacillus brevis at elevated temperatures," in *Industry Applications Society Annual Meeting, 1991., Conference Record of the 1991 IEEE*, 1991, pp. 674-681 vol.1.
[83] B. Rubinsky, "Micro-electroporation in cellomics," in *Lab-on-Chips for Cellomics*, ed, 2004, pp. 123-141.
[84] Y. C. Lin and M. Y. Huang, "Electroporation microchips for in vitro gene transfection," *Journal of Micromechanics and Microengineering,* vol. 11, pp. 542-547, Sep 2001.
[85] Y. C. Lin*, et al.*, "Electroporation microchips for continuous gene transfection," *Sensors and Actuators B-Chemical,* vol. 79, pp. 137-143, Oct 2001.

[86] Y. Huang and B. Rubinsky, "Micro-Electroporation: Improving the Efficiency and Understanding of Electrical Permeabilization of Cells," *Biomedical Microdevices,* vol. 2, pp. 145-150, 1999.

[87] Y. Huang and B. Rubinsky, "Microfabricated electroporation chip for single cell membrane permeabilization," *Sensors and Actuators A: Physical,* vol. 89, pp. 242-249, 2001.

[88] Y. Huang and B. Rubinsky, "Flow-through micro-electroporation chip for high efficiency single-cell genetic manipulation," *Sensors and Actuators A: Physical,* vol. 104, pp. 205-212, 2003.

[89] J. A. Lundqvist*, et al.*, "Altering the biochemical state of individual cultured cells and organelles with ultramicroelectrodes," *Proc Natl Acad Sci U S A,* vol. 95, pp. 10356-60, Sep 1 1998.

[90] J. Gao*, et al.*, "Integration of single cell injection, cell lysis, separation and detection of intracellular constituents on a microfluidic chip," *Lab on a Chip,* vol. 4, pp. 47-52, 2004.

[91] S.-W. Lee and Y.-C. Tai, "A micro cell lysis device," *Sensors and Actuators A: Physical,* vol. 73, pp. 74-79, 1999.

[92] J. Suehiro*, et al.*, "High sensitive detection of biological cells using dielectrophoretic impedance measurement method combined with electropermeabilization," *Sensors and Actuators B: Chemical,* vol. 96, pp. 144-151, 2003.

[93] M. Fox*, et al.*, "Electroporation of cells in microfluidic devices: a review," *Analytical and Bioanalytical Chemistry,* vol. 385, pp. 474-485, 2006.

[94] T. Ohshima and M. Sato, "Bacterial Sterilization and Intracellular Protein Release by a Pulsed Electric Field," in *Recent Progress of Biochemical and Biomedical Engineering in Japan I*, ed, 2004, pp. 760-760.

[95] A. O. Bilska*, et al.*, "Theoretical modeling of the effects of shock duration, frequency, and strength on the degree of electroporation," *Bioelectrochemistry,* vol. 51, pp. 133-143, 2000.

[96] M. P. Rols and J. Teissié, "Electropermeabilization of mammalian cells. Quantitative analysis of the phenomenon," *Biophysical Journal,* vol. 58, pp. 1089-1098, 1990.

[97] M. Takahashi*, et al.*, "Gene transfer into human leukemia cell lines by electroporation: Experience with exponentially decaying and square wave pulse," *Leukemia Research,* vol. 15, pp. 507-513, 1991.

[98] K. Nolkrantz*, et al.*, "Electroporation of Single Cells and Tissues with an Electrolyte-filled Capillary," *Analytical Chemistry,* vol. 73, pp. 4469-4477, 2001.

[99] K. Haas*, et al.*, "Single-cell electroporation for gene transfer in vivo," *Neuron,* vol. 29, pp. 583-91, Mar 2001.

[100] M. Khine*, et al.*, "Single-cell electroporation arrays with real-time monitoring and feedback control," *Lab on a Chip,* vol. 7, pp. 457-462, 2007.

[101] D. Nawarathna*, et al.*, "Localized electroporation and molecular delivery into single living cells by atomic force microscopy," *Applied Physics Letters,* vol. 93, pp. 153111-3, 2008.

[102] K. Nolkrantz*, et al.*, "Functional Screening of Intracellular Proteins in Single Cells and in Patterned Cell Arrays Using Electroporation," *Analytical Chemistry,* vol. 74, pp. 4300-4305, 2002.

[103] Q. Zheng and D. C. Chang, "HIGH-EFFICIENCY GENE TRANSFECTION BY INSITU ELECTROPORATION OF CULTURED-CELLS," *Biochimica Et Biophysica Acta,* vol. 1088, pp. 104-110, Jan 1991.

[104] G. W. Grime and F. Watt, *Beam optics of quadrupole probe-forming systems / G.W. Grime, F. Watt*. Bristol [Avon] :: Hilger, 1984.

[105] J. A. van Kan*, et al.*, "Fabrication of a free standing resolution standard for focusing MeV ion beams to sub 30 nm dimensions," *Nuclear Instruments and Methods in Physics*

Research Section B: Beam Interactions with Materials and Atoms, vol. 231, pp. 170-175, 2005.

[106] A. A. Bettiol*, et al.*, "A LabVIEW(TM)-based scanning and control system for proton beam micromachining," *Nuclear Instruments and Methods in Physics Research Section B: Beam Interactions with Materials and Atoms,* vol. 181, pp. 49-53, 2001.

[107] A. A. Bettiol*, et al.*, "Ionscan: scanning and control software for proton beam writing," *Nuclear Instruments and Methods in Physics Research Section B: Beam Interactions with Materials and Atoms,* vol. 231, pp. 400-406, 2005.

[108] J. A. van Kan*, et al.*, "Hydrogen silsesquioxane a next generation resist for proton beam writing at the 20 nm level," *Nuclear Instruments and Methods in Physics Research Section B: Beam Interactions with Materials and Atoms,* vol. 260, pp. 396-399, 2007.

[109] D. Kauzlarick, "Fundamentals of microfabrication, the science of miniaturization, 2nd edition [Book Review]," *Engineering in Medicine and Biology Magazine, IEEE,* vol. 22, pp. 109-111, 2003.

[110] S. Y. Chiam*, et al.*, "Sidewall quality in proton beam writing," *Nuclear Instruments & Methods in Physics Research Section B-Beam Interactions with Materials and Atoms,* vol. 260, pp. 455-459, Jul 2007.

[111] J. van Kan*, et al.*, "Proton beam writing: a progress review," *International Journal of Nanotechnology,* vol. 1, pp. 464-479, 2004.

[112] F. Watt*, et al.*, "Proton beam micromachined resolution standards for nuclear microprobes," *Nuclear Instruments and Methods in Physics Research Section B: Beam Interactions with Materials and Atoms,* vol. 190, pp. 306-311, 2002.

[113] D. Spemann*, et al.*, "Suitable test structures for submicron ion beam analysis," *Nuclear Instruments and Methods in Physics Research Section B: Beam Interactions with Materials and Atoms,* vol. 190, pp. 312-317, 2002.

[114] F. Zhang*, et al.*, "Fabrication of free standing resolution standards using proton beam writing," *Nuclear Instruments and Methods in Physics Research Section B: Beam Interactions with Materials and Atoms,* vol. 260, pp. 474-478, 2007.

[115] J. L. Sanchez*, et al.*, "A high resolution beam scanning system for deep ion beam lithography," *Nuclear Instruments and Methods in Physics Research Section B: Beam Interactions with Materials and Atoms,* vol. 136-138, pp. 385-389, 1998.

[116] J. A. van Kan*, et al.*, "Resist materials for proton micromachining," *Nuclear Instruments and Methods in Physics Research Section B: Beam Interactions with Materials and Atoms,* vol. 158, pp. 179-184, 1999.

[117] Y. Tsuru*, et al.*, "Effects of boric acid on hydrogen evolution and internal stress in films deposited from a nickel sulfamate bath," *Journal of Applied Electrochemistry,* vol. 32, pp. 629-634, 2002.

[118] J. Garcia-Perez*, et al.*, "Lithium induces morphological differentiation of mouse neuroblastoma cells," *J Neurosci Res,* vol. 57, pp. 261-70, Jul 15 1999.

[119] B. Roth*, et al.*, "Bacterial viability and antibiotic susceptibility testing with SYTOX green nucleic acid stain," *Appl. Environ. Microbiol.,* vol. 63, pp. 2421-2431, June 1, 1997 1997.

[120] M. W. Jernaes and H. B. Steen, "STAINING OF ESCHERICHIA-COLI FOR FLOW-CYTOMETRY - INFLUX AND EFFLUX OF ETHIDIUM-BROMIDE," *Cytometry,* vol. 17, pp. 302-309, Dec 1994.

[121] E. S. Kaneshiro*, et al.*, "RELIABILITY OF CALCEIN ACETOXY METHYL-ESTER AND ETHIDIUM HOMODIMER OR PROPIDIUM IODIDE FOR VIABILITY ASSESSMENT OF MICROBES," *Journal of Microbiological Methods,* vol. 17, pp. 1-16, Jan 1993.

[122] R. Lopezamoros*, et al.*, "FLOW CYTOMETRIC ASSESSMENT OF ESCHERICHIA-COLI AND SALMONELLA-TYPHIMURIUM STARVATION-SURVIVAL IN

SEAWATER USING RHODAMINE-123, PROPIDIUM IODIDE, AND OXONOL," *Applied and Environmental Microbiology,* vol. 61, pp. 2521-2526, Jul 1995.

[123] J. D. Mansour*, et al.*, "FLUORESCENT STAINING OF INTRACELLULAR AND EXTRACELLULAR BACTERIA IN BLOOD," *Journal of Clinical Microbiology,* vol. 19, pp. 453-456, 1984.

[124] L. A. Vanderwaaij*, et al.*, "DIRECT FLOW-CYTOMETRY OF ANAEROBIC-BACTERIA IN HUMAN FECES," *Cytometry,* vol. 16, pp. 270-279, Jul 1994.

[125] S. Langsrud and G. Sundheim, "Flow cytometry for rapid assessment of viability after exposure to a quaternary ammonium compound," *Journal of Applied Bacteriology,* vol. 81, pp. 411-418, Oct 1996.

[126] C. Chen*, et al.*, "Membrane electroporation theories: a review," *Med Biol Eng Comput,* vol. 44, pp. 5-14, Mar 2006.

[127] E. G. Guignet and T. Meyer, "Suspended-drop electroporation for high-throughput delivery of biomolecules into cells," *Nat Meth,* vol. 5, pp. 393-395, 2008.

[128] J. Garcia-Perez*, et al.*, "Lithium induces morphological differentiation of mouse neuroblastoma cells," *Journal of Neuroscience Research,* vol. 57, pp. 261-270, Jul 1999.

[129] C. Udalagama*, et al.*, "Stochastic spatial energy deposition profiles for MeV protons and keV electrons," *Physical Review B,* vol. 80, p. 224107, 2009.

[130] J. W. Lichtman and J.-A. Conchello, "Fluorescence microscopy," *Nat Meth,* vol. 2, pp. 910-919, 2005.

[131] M. Fernandez-Suarez and A. Y. Ting, "Fluorescent probes for super-resolution imaging in living cells," *Nat Rev Mol Cell Biol,* vol. 9, pp. 929-943, 2008.

[132] W. Reitz, "Materials Analysis Using a Nuclear Microprobe M. B. H. Breese, D. N. Jamieson, and P. I. C. King," *Materials and Manufacturing Processes,* vol. 13, pp. 159 - 160, 1998.

[133] D. Needham and R. M. Hochmuth, "Electro-mechanical permeabilization of lipid vesicles. Role of membrane tension and compressibility," *Biophysical Journal,* vol. 55, pp. 1001-1009, 1989.

[134] J. Akinlaja and F. Sachs, "The breakdown of cell membranes by electrical and mechanical stress," *Biophys J,* vol. 75, pp. 247-54, Jul 1998.

Appendices

Appendix A

HAMAMATSU Metal Package Photomultiplier Tube (PMT) R7402

R7402 is in the R7400U series of Hamamatsu metal package photomultiplier tube. This series is a subminiature photomultiplier tube with a 16 mm diameter and 2 mm seated length. A precision engineered 8-atage electron multiplier (composed of metal channel dynodes) is incorporated in the TO-8 package to produce a noise free gain of 700,000 times. The R7400U series also features excellent response time with a rise time of 0.78 ns. The R7402 is one of the option that provides a lens input, effectively doubling the active area.

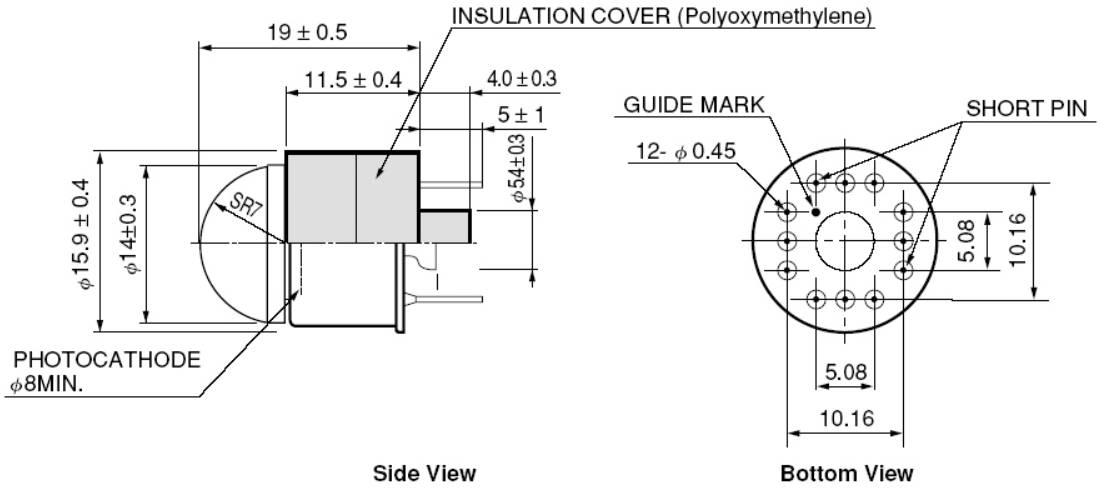

Figure A.1 The drawing of the side view and bottom view of the PMT

Table A.1 Key Specifications

Part Number	R7402
Type	Metal
Size	16mm
ActiveDia/L	8mm
Min λ	300nm
Max λ	850nm
Peak Sens.	400nm
Cathode Radiant Sensitivity	60mA/W
Window	Borosilicate
Cathode Type	Multialkali
Cathode Luminous Sensitivity	150mA/lm
Red White Ratio	200
Anode Luminous Sensitivity	75A/lm
Gain	5.0E+05
Dark Current after 30 min.	0.4nA
Rise Time	0.78ns
Transit Time	5.4ns
Transit Time Spread	0.28ns
Number of Dynodes	8
Applied Voltage	800V
Multi Anode	N
Notes	Compact size. fast response time. smallest photomultiplier tube
Socket Bare	E678-12V
Socket + bleeder assy.	E5770 E5780
Socket + bleeder + Amp.	C5781
Power Supply	C4840 series C3360
Amplifier	C7319 C6438 C5594 M7279 M8879

Appendix B

Publications

[1] S. Homhuan, B. Zhang, F. Sheu. A.A. Bettiol and F. Watt, "Single cell electroporation using proton beam fabricated biochips" Proceedings of SPIE Vol. 7716, 77160V (2010).

[2] C. N. B. Udalagama, S.F. Chan, S. Homhuan, S., A.A. Bettiol and F. Watt, "Fabrication of integrated channel waveguides in polydimethylsiloxane (PDMS) using proton beam writing (PBW): applications for fluorescence detection in microfluidic channels," Proceedings of SPIE Vol. 6882, 68820D (2008).

Abstracts presented at conferences

[1] S. Homhuan, B. Zhang, F. Sheu. A.A. Bettiol and F. Watt, "Single cell electroporation using proton beam fabricated biochips" SPIE Photonics Europe 2010, Brussels, Belgium 12-16 April 2010 (Oral presentation).

[2] S. Homhuan, B. Zhang, F. Sheu. A.A. Bettiol and F. Watt, "Single cell electroporation using proton beam fabricated biochips" Scinece and Technology for a Sustainable Future, Bangkok, Thailand 7-9 Decenber 2009 (Poster presentation)

[3] S. Homhuan, H. F. Cui, B. Shang, F. Sheu. A.A. Bettiol and F. Watt, " Single-cell electroporation using proton beam fabricated biochips " International Conference on Materials for Advanced Technologies (ICMAT) 2009, Singapore 28 June- 3 July 2009 (Oral presentation)